



Microstructural Study of Cold-Sprayed CoCrFeNiMn High Entropy Alloy

Cletus J. Akisin¹ · Bogdan Dovggy² · Christopher J. Bennett³ · Minh-Son Pham² · Federico Venturi¹ · Tanvir Hussain¹

Submitted: 23 April 2023 / in revised form: 5 July 2023 / Accepted: 7 August 2023 / Published online: 22 August 2023
© The Author(s) 2023

Abstract The rapid development of cold spraying technology for additive manufacturing of engineering components has made it a viable option for developing thick deposits from high-entropy alloys (HEAs). The microstructure of cold-sprayed CoCrFeNiMn deposit was investigated in this study using electron backscattered diffraction, scanning electron microscopy, and finite element analysis (FEA). The limited studies on the impact deformation behavior of the HEA during cold spraying, limiting our understanding of impact phenomena, and interactions between the HEA particles under ultra-high strain rate deformation motivated this study. From the microstructural characterization, heterogeneous microstructure appears to be formed in the cold-sprayed HEA deposit, comprising of equiaxed ultrafine grains at the particle–particle interfacial regions and coarse grains at the particle interiors. The FEA reveals large strain (> 250%) and temperature (> 90% of the alloy solidus temperature), mainly at the splat’s interfaces. Adiabatic shear instability and rotational dynamic recrystallization resulting from heat accumulation and high strain are believed to be responsible for these observations during the ultra-high strain rate deformation of the HEA. The large deformation and grain

refinement experienced by the HEA resulted in greater deposit hardness when compared with the sprayed powder, with the nanohardness increasing from 1.16 GPa in the powder to 5.14 GPa in the deposit. This study explores and provides an understanding of the deformation behavior of the HEA and the resulting microstructure during cold spraying.

Keywords adiabatic shear instability · cold spray additive manufacturing · dynamic recrystallization · finite element analysis · high-entropy alloys

Introduction

In recent years, targeted attention has been raised to developing zero-carbon emission systems, such as in aerospace, automotive, and nuclear systems. The development of these systems calls for the development of high-performance alloys with exceptional mechanical properties, such as a good combination of high strength and ductility, excellent fracture toughness, and resistance to hydrogen embrittlement. High-entropy alloys (HEAs), a new class of metallic alloys first introduced in 2004 (Ref 1, 2) with good mechanical properties (Ref 3), provide an excellent opportunity to develop high-performance alloys that would meet the requirement for developing clean-energy systems. The underlying mechanism behind HEAs is that the presence of multiple elements near equal-atomic proportions would increase the entropy of mixing to a sufficient amount able to overcome the enthalpy of mixing, resulting in the formation of solid solutions and simple crystal structures (Ref 2). As a representative HEA, the CoCrFeNiMn, which forms a solid solution with a single-phase FCC crystal structure, has been the first and most

✉ Cletus J. Akisin
eaxca2@nottingham.ac.uk

✉ Tanvir Hussain
Tanvir.Hussain@nottingham.ac.uk

¹ Coatings and Surface Engineering, Faculty of Engineering, University of Nottingham, Nottingham NG7 2RD, UK

² Department of Materials, Imperial College London, Exhibition Road, South Kensington, London SW7 2AZ, UK

³ Rolls-Royce UTC, University of Nottingham, Nottingham NG7 2RD, UK

studied HEA. The attractive properties of this HEA are its excellent strength and ductility combination (Ref 4, 5), exceptional fracture toughness at cryogenic and room temperatures (Ref 6) and resistance to hydrogen embrittlement (Ref 7). These properties have motivated several researchers to improve the strength of the HEA for practical applications by tuning its microstructures via various processes (Ref 8).

Over the past decades, the thermomechanical treatment of the CoCrFeNiMn HEA, including severe plastic deformation (SPD) followed by annealing at intermediate temperatures, has been demonstrated to result in improved strength (Ref 8); however, some studies have demonstrated the detrimental effect of brittle phase formation on the ductility of the HEA heat-treated at intermediate temperatures (Ref 9, 10). High-pressure torsion (HPT) (Ref 11) and equal-channel angular pressing (ECAP) (Ref 12) are examples of technologies for imposing SPD of the HEA to achieve substantial grain refinement from sub-micrometer to nano-meter scale. Ultrafine grains produced via these SPD processes can, however, result in limited ductility of the component.

One way to achieve an excellent combination of high strength and ductility of this HEA is by forming heterogeneous microstructures without requiring subsequent heat treatment. Cold spray (CS) is a solid-state and ultra-high strain rate materials deposition technique that can promote the formation of heterogeneous microstructures (Ref 13–15). For instance, Singh et al. (Ref 13) and Chen et al. (Ref 14) fabricated a thick Cu deposit with heterogeneous microstructures with elongated coarse grains at the particle interiors and ultrafine grains at inter-particle regions. The deposits exhibited high ductility and strength without the need for heat treatment, where the ultrafine grains provide high strength, but the coarse grains could accommodate many dislocations resulting in decent ductility. However, there are limited studies on the formation of these microstructures developed in the HEA, which can result from the ultra-high strain rate deformation of the alloy using the CS process (Ref 16–20).

CS technology has recently been recognized as a new solid-state additive manufacturing (AM) technique for producing metallic components, called cold spray additive manufacturing (CSAM). This technique relies on the kinetic energy of the feedstock powder particles to develop deposits layer by layer. The feedstock powder particles, typically about 5–50 μm in diameter, are accelerated in a jet of compressed gas (N_2 , He or air) to high velocities ranging from 300 to 1400 m/s through a de-Laval nozzle (Ref 21, 22). Deposits are then formed through the plastic deformation of the powder particles at an ultra-high strain

rate (10^7 – 10^9 s^{-1}), consequently bonding to the substrate when the particle impact velocity reaches a material-dependent critical velocity. Given these, CSAM offers unique advantages over other AM techniques where thermal energy is the primary principle for materials deposition, such as laser-based AM (Ref 14–17). Also, CSAM, being a solid-state process, avoids the oxidation and phase changes of the microstructure of HEA deposits (Ref 16, 17, 20). CSAM can also provide the capability for the in situ repair of aerospace components (Ref 23–25) due to its excellent process economy and flexibility for usage; however, the CS repair process has not been explored with HEAs.

Furthermore, the time scale and contact nature of the CSAM process make it difficult to investigate the interactions between particles and substrates during deposition. Consequently, post-mortem microstructural and micro-analytical examinations using several techniques are performed to investigate the interactions between particles, impact deformation behavior, and microstructural features after CS. As a result, finite element analysis (FEA) is employed to analyze the interactions of particles between themselves and substrates (Ref 26, 27). Over the past decades, using different FEA tools has enhanced the understanding of particle and particle-to-substrate interactions (Ref 27–31) and the resulting microstructure, such as grain refinement resulting from the large strain, high strain rates, and temperatures at impact regions during cold spraying (Ref 15). However, there are limited reports on the impact deformation behavior of the CoCrFeNiMn HEA during cold spraying using FEA tools. So far, single-particle impact deformation modeling has been reported (Ref 32); however, no reports on multi-particle impact deformation modeling of the HEA exist, limiting our understanding of the impact deformation behavior of the HEA during ultra-high strain rate deformation via CS. In addition, FEA multi-particle deformation model and the experimental microstructural analysis would provide insight into the interaction between HEA particles when developing deposits layer by layer and enabling the manufacturing of HEA components with dense heterogeneous microstructures via the CSAM process.

The CoCrFeNiMn HEA was deposited in this study using the cold spraying process. The microstructure evolution from the feedstock powder to the cold-sprayed deposit of the HEA was performed using SEM, EBSD, and XRD. During cold spraying, the particle-to-particle and particle-to-substrate interactions were investigated via finite element modeling. The mechanical properties of the deposit were evaluated using micro- and nanohardness testing.

Methodology

Materials and Experimental Methods

Nearly equiatomic pre-alloyed spherical gas-atomized CoCrFeNiMn HEA powder provided by HC Starck Surface Technology and Ceramic Powders GmbH (Germany) was the feedstock material used in this study. A laser diffractometer (LA-960, Horiba Scientific, Japan) with a 650-nm laser diode was used to obtain the powder particle size distribution. Before measurement, a small representative of the powder sample was dispersed in a wet medium and ultrasonicated to avoid particle agglomeration.

A high-pressure CS system developed at the University of Nottingham was employed for the deposition of the HEA powder feedstock, with the spraying parameters provided in Table 1. The powder carrier gas was set at 0.1 MPa higher than the accelerating gas pressure. The cold spray nozzle was made of hardened stainless steel, designed with an area expansion ratio of ~ 9 , a throat diameter of 1.35 mm, and a divergent length of 150 mm. The cold spray deposition system was stationary, while the substrates were mounted on a programmable x–y table that allowed a controllable scan pattern and velocity. The substrate used for the deposition was a 2-mm-thick austenitic stainless steel AISI304 (SS304) plate (25 × 60 mm) with a nominal composition of 19.0 wt.% Cr, 9.3 wt.% Ni, and 0.05 wt.% C, with the remainder being Fe. The substrate was ground with P240 SiC grit paper before spraying to enhance the adhesion of the deposit during the CSAM.

The feedstock powder and the cold-sprayed cross-sectioned samples were cold-moulded using EpoFin® epoxy resin (Struers, UK). Powders were ground using P800 to P4000 SiC grinding papers with final polishing with a 0.04- μm colloidal silica suspension. The cold-sprayed samples were ground using P240 to P4000 SiC grinding papers. Mechanical polishing down to 1 μm using diamond paste

was performed for porosity evaluation of the cold-sprayed deposit. For further characterization of the cold-sprayed deposit, final polishing was done using a vibratory polisher with a 0.04- μm colloidal silica suspension mixed with 7 vol.% of H_2O_2 . All samples were washed and cleaned with ethanol between each grinding and polishing step.

The morphology of the feedstock powder particles was observed using an SEM (XL30, FEI, The Netherlands), and the chemical composition of the cross-sectioned powder sample was evaluated using an energy dispersive x-ray (EDX) detector (Oxford Instrument, UK) mounted on the SEM. The microstructure of the cold-sprayed deposit was observed using the SEM operated at 15 kV in the backscattered electron (BSE) mode. The porosity and thickness of the deposit were quantified by image analysis using the greyscale thresholding technique in the ImageJ software (NIH, USA). Five BSE SEM images were used to measure the thickness of the deposit, while ten BSE SEM images were used to measure the porosity. The images were captured at $\times 500$ magnification, resulting in a field of view with an area of $100 \times 100 \mu\text{m}^2$. The results are presented as average values with the standard error.

X-ray diffraction (XRD) was conducted on a D8 Advance Da Vinci x-ray diffractometer (Bruker, Germany), with a wavelength of 0.15406 nm (Cu-K_α), in Bragg–Brentano θ - 2θ geometry, 20° to 80° , a step of $0.02^\circ 2\theta$ and 0.1 s dwell time. The crystal structure identification of the powder and deposit from the XRD profiles were completed using the EVA software (DIFFRAC.EVA, Bruker, Germany) with the ICDD database PDF 2.

To observe the morphology and measure the size of the grains in the powder, EBSD was performed on a FEG SEM (7100F, JEOL Ltd., Japan) with a specimen tilt angle of 70° , operated at an accelerating voltage of 15 kV with a step size of 0.2 μm , exposure time of 100 ms, at a working distance of 16 mm and detector insertion distance of 193 mm. The EBSD of the deposit was performed on a Zeiss™ Auriga Cross Beam SEM (Germany) equipped with a high-resolution (HR) EBSD detector at an accelerating voltage of 20 kV, an aperture size of 60 μm , a working distance of 18 mm, a detector distance of 10 mm, an exposure time of 15 ms, with a step size of 0.05 μm . The EBSD scans of the powder sample and post-processing data were carried out using Aztec and AZtecCrystal software (Oxford Instruments, UK). Detailed analysis of the EBSD maps of deposited samples was performed using the MTEX toolbox. The geometrically necessary dislocation (GND) density was estimated following Pantleon's methodology (Ref 33). The elemental distribution in the feedstock powder was studied using EDX mapping in the FEG SEM equipped with the X-max 150 EDX detector (Oxford, Instruments, UK).

Table 1 Cold spraying process parameters for the deposition of CoCrFeNiMn HEA

Spraying parameters	Values
Accelerating gas	He
Gas pressure, MPa	3.3
Gas temperature, $^\circ\text{C}$	400
Nozzle transverse speed, mm/s	100
Increment size, mm	2
Stand-off distance, mm	20
Number of passes	4
Powder feed rate, g/min	42

The nanohardness of the feedstock powder and deposit was measured using a NanoTest P3 nano-indenter (Micro Materials Ltd., UK). Each sample underwent at least ten measurements on the powder particles and an array (20×20) of 400 indents on the cold-sprayed deposits. A Berkovich indenter was used to test the nanohardness measurement, with a 3-mN peak load, 10 s dwell time, and 0.75 mN/s loading/unloading rate. This indentation load was chosen after carefully selecting the indent size, the distance between the neighboring indents ($7 \mu\text{m}$) to account for the plastic zone or indent impression, and the distance between indents and the cold spray splats boundaries to avoid pores when indenting the cold-sprayed deposit. The nanohardness (H) and reduced modulus (E_r) from the nano-indenter are derived following the Oliver and Pharr method (Ref 34), determined using Eqs 1 and 2, where P_m is the maximum applied load (in mN), A is the projected contact area, and S is the contact stiffness (in $\mu\text{N}/\text{nm}$). The elastic modulus of the deposit, E_c , was obtained using the expression in Eq 3, considering the Poisson ratio, V_i (0.07), and Young's modulus, E_i (1140 GPa), of the Berkovich indenter diamond tip (Ref 35). The final values were presented as an average with the standard error.

$$H = P_m/A \quad (\text{Eq 1})$$

$$E_r = \frac{\sqrt{\pi} S}{2 A} \quad (\text{Eq 2})$$

$$1/E_r = \left(1 - V_c^2/E_c\right) + \left(1 - V_i^2/E_i\right) \quad (\text{Eq 3})$$

The microhardness of the deposit was also measured using a Wilson VH3300 Vickers Microhardness instrument (Buehler, USA). The deposit sample underwent an array of 280 micro-indents. A 300-gf load was applied on the deposit, using a dwell time of 15 s. The final value is presented as an average with the standard error.

Computational Methods

The impact behavior of high-velocity, micro-sized HEA particles onto the SS304 substrate was modeled using the Lagrangian approach with the Abaqus/Explicit commercial code. Two-dimensional (2D) model was used to simulate the multi-particle deformation behavior of the HEA material on the substrate. The 2D multi-particle model was defined as a plane strain model containing 50 particles with sizes between 10 and $45 \mu\text{m}$ distributed randomly, as shown in Fig. 1. This was employed to characterize the deformation in the deposit's center cross section. More so, the number of particles was selected when considering the smallest region or field of view of the microstructure observed with the SEM. The substrate was modeled as a cylinder having a height and radius of $450 \mu\text{m}$ and $800 \mu\text{m}$,

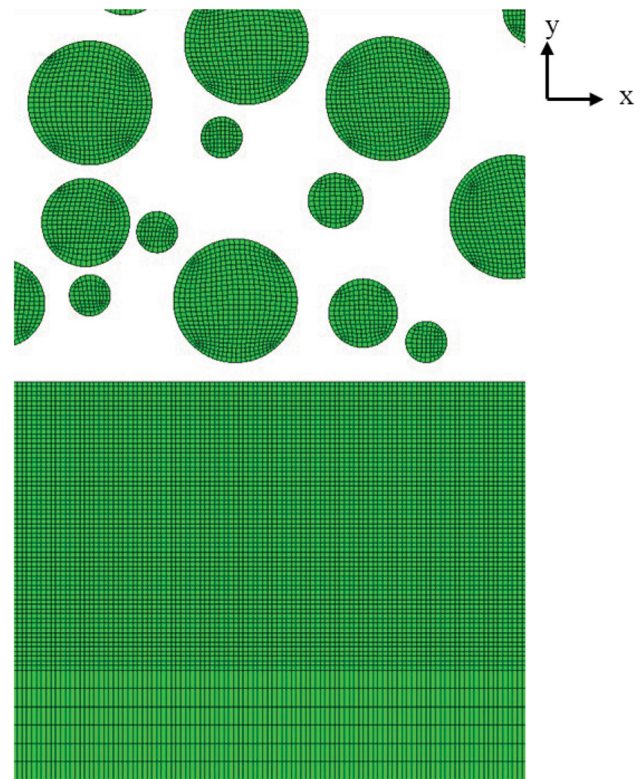


Fig. 1 Abaqus computational domain for the multi-particle impact model. The figure shows a closer view cut-out at the center of the domain, showing the meshing of the particles and substrate

respectively. The fixed boundary condition and X-displacement constraint were applied to the bottom of the substrate and sidewalls. A four-node plane strain thermally coupled quadrilateral, bilinear displacement and temperature, reduced integration, and hourglass control elements (CPE4RT) were used to mesh the model. Following our previous work (Ref 32), the particles and substrate impact zone used a mesh size of $0.4 \mu\text{m}$. The simulation was run for $1 \mu\text{s}$ to capture the whole deformation process.

A surface-to-surface penalty contact algorithm was specified for all interface regions, with a friction coefficient of 0.3 assumed for all cases (Ref 36). All model contact surfaces were constrained to remain in contact during the impact process. The shape of the particles was assumed to be perfectly spherical, and impacts were normal to the substrate surface.

The FEA accounted for strain hardening, strain rate hardening, thermal softening, and heating due to friction, plastic, and viscous dissipation. The non-adiabatic condition considered in previous studies (Ref 30, 37, 38) was employed in this model; that is, a dynamic temperature displacement explicit procedure (coupled thermal-mechanical analysis) was performed, and it was assumed that 90% of the kinetic energy of the model dissipated into heat, allowing for heat transfer and stored energy. The thermal

response of the materials was described by specific heat capacity and thermal conductivity. The elastic response of the materials was defined by the elastic modulus and Poisson’s ratio, while the plastic deformation behavior was determined using the Johnson–Cook (J–C) plasticity model (Ref 39). The J–C plasticity model of metallic materials is mainly applied to transient nonlinear dynamic simulations. The material is assumed to be isotropic linear-elastic, strain rate-sensitive, strain-hardenable, and thermally softenable plastic material (Ref 39, 40). The J–C material model utilizes the J_2 yield function, expressing the stresses according to the von Mises yield criterion. The flow stress (σ) is defined as follows:

$$\sigma = [A + B\varepsilon^n][1 + C\ln(\dot{\varepsilon}^*)][1 - \theta^m] \tag{Eq 4}$$

where ε is the equivalent plastic strain, and $\varepsilon^* = \dot{\varepsilon}/\dot{\varepsilon}_0$, $\dot{\varepsilon}$ is the equivalent plastic strain rate, $\dot{\varepsilon}_0$ is the reference plastic strain rate, A is the yield strength (MPa) at zero-plastic strain and at room temperature, B is the strain hardening (MPa), n is the strain hardening exponent, C is the strain rate constant, and m is the thermal softening exponent. Also, the temperature effect of the J–C model given in the last part of Eq. 4 accounts for the thermal softening of the material at a high strain rate, and θ is given as,

$$\theta = \frac{T - T_{\text{ref}}}{T_{\text{melt}} - T_{\text{ref}}} \tag{Eq 5}$$

where T is the homologous material temperature, T_{ref} is the reference temperature, and T_{melt} is the material melting temperature. The increase in temperature T resulting from adiabatic temperature rise is given by Eq 6, where ρ is the material density, β is the inelastic heat fraction taken as 0.9, and C_p is the specific heat capacity of the material. The selection of the J–C material parameters that best predict the deformation morphology of a single-particle impact of the HEA material on various substrates has been reported in a previous study (Ref 32); thus, the J–C material parameters used for the HEA particle and SS304 substrate in this study are provided in Table 2.

$$T = T_{\text{ref}} + \frac{\beta}{\rho C_p} \int_0^\varepsilon \sigma d\varepsilon \tag{Eq 6}$$

The particle velocities and temperatures in Fig. 2 were defined as input parameters to the Abaqus impact model. They were predicted following the experimental spraying conditions in Table 1 and the nozzle dimensions using a simplified 2D axisymmetric computational fluid dynamics (CFD) model with the commercial code of Fluent (Ansys Fluent, version 2020). This detail can be found in (Ref 32). Spherical CoCrFeNiMn particles from 5 to 45 μm , with an initial temperature of 25 $^\circ\text{C}$ were used as powders injected at the nozzle inlet. The CFD analysis revealed that the

Table 2 The HEA and substrate material data and Johnson-Cook plasticity constants used for this study

Material properties	CoCrFeNiMn	SS304
Density, ρ , kg/m^3	7958	8000
Elastic modulus, E , GPa	202	207.8
Poisson ration, ν	0.265	0.3
A , MPa	590	280
B , MPa	1365	802.5
n	0.18	0.622
C	0.028	0.0799
m	0.7	1.0
Reference strain rate	1	1
Melting temperature, T_{melt} , K	1600	1673
Reference temperature, T_{ref}	473	298
Specific heat capacity, J/KgK	430	452
Thermal conductivity, W/mK	12	16.2

increase in particle size increases the particle temperature before deposition, which is the opposite for the case of particle velocity: Velocity decreases while temperature increases as the particle size increases. Since the CFD results are likely to deviate from the actual experimental particle velocity and temperature (Ref 41-43), a 15% deviation from the CFD results is employed. At the spraying conditions in Table 1, the estimated particle velocities for the particle size range from 15 to 45 μm would be from 1063 to 704 m/s. Thus, the average particle velocity (i.e., for a particle size of 25 μm) was \sim 885 m/s.

Results

Powder Microstructures

Figure 3(a) shows the surface morphology of the feedstock powder. The gas-atomized HEA feedstock powder exhibits a predominately spherical morphology, accompanied by irregular particles with satellites attached to them (Fig. 3a), typical for gas-atomized powders (Ref 44). The larger particle shown in Fig. 3(a) reveals a dendritic structure. The micrographs of the HEA feedstock powder obtained from the EBSD and grain size analysis are presented in Fig. 4. Figure 4(a) represents the EBSD inverse pole figure (IPF) map of a HEA feedstock powder particle. The IPF-z map, with different colors representing the grain orientations, reveals several randomly oriented grains with different shapes and sizes within the HEA particle. The powder particle microstructure appears to consist of a mixture of columnar and equiaxed grains, likely growing

Fig. 2 The results of the CFD simulations of the HEA particle velocity and temperature as a function of the particle size

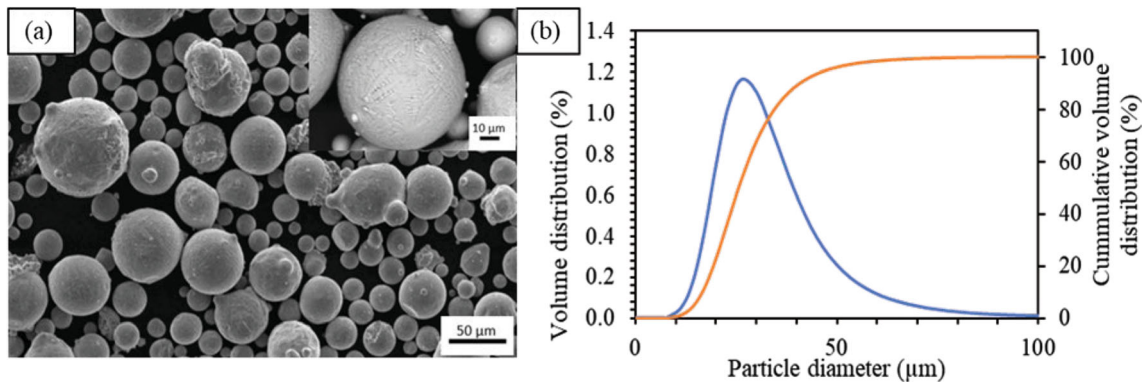
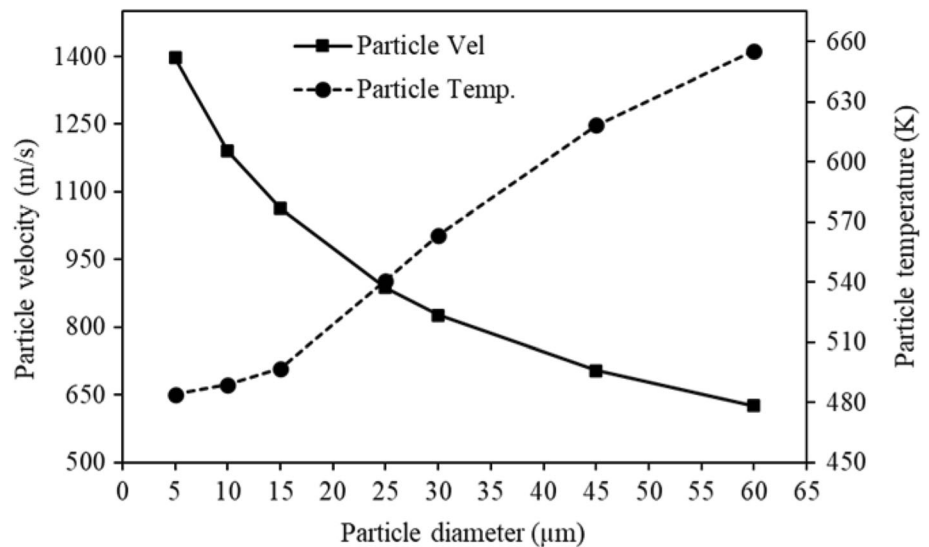


Fig. 3 The SEM micrograph of the CoCrFeNiMn HEA powder particle surface morphology (a) with a magnified view of the BSE micrograph of a single-particle and the powder particle size distribution (b)

outwards from the nucleation point (Fig. 4a). These features likely result from the undercooling and dendrite break-up during the gas-atomization process (Ref 45). Few poorly indexed grains at the particle edges can be seen, attributed to polishing artifacts. Figure 4(b) shows the size distribution of the grains in the HEA powder particles with an area-weighted average grain size of about 6–7 μm. EDX mapping of the elemental composition of the HEA powder particles is presented in Fig. 4(c), showing microsegregation of Co, Cr, and Fe in the dendritic interiors, which has also been observed in a previous study (Ref 46). The chemical composition of the powder is 22.3 wt.% Co, 19.3 wt.% Cr, 20.1 wt.% Fe, 20.7 wt.% Ni, and 17.6 wt.% Mn.

Deposit Porosity and Inter-particle Bonding

SEM micrographs of the CoCrFeNiMn HEA deposit cross sections on the substrate at various magnifications are shown in Fig. 5. The low-magnification micrograph in Fig. 5(a) presents a (1.67 ± 0.03) -mm-thick deposit

showing no discontinuity or delamination at the deposit–substrate interface, indicating a good bonding between the deposit and the substrate during the CSAM. A porosity of $(2.4 \pm 0.3)\%$ was measured in the deposit. Higher magnification micrographs of the deposit cross sections in Fig. 5(b) and (c) reveal a nearly homogenous distribution of pores.

As a representative of the deposit cross section, the SEM micrograph and numerical simulation of the multi-particle impact model (2D model) of the HEA particles on the substrate are presented in Fig. 6(a), (b), and (c), respectively. The deposit microstructure shown in Fig. 6(a) and (b) consists of splats with globular or oblate spheroid morphology, and similar deformation morphology is observed in the FEA model. This suggests that the FEA model employed thus represents the HEA particle deformation morphology well.

Further, a broad distribution of the splat size within the deposit microstructure was observed, correlating with the characteristic particle size distribution of the HEA powder,

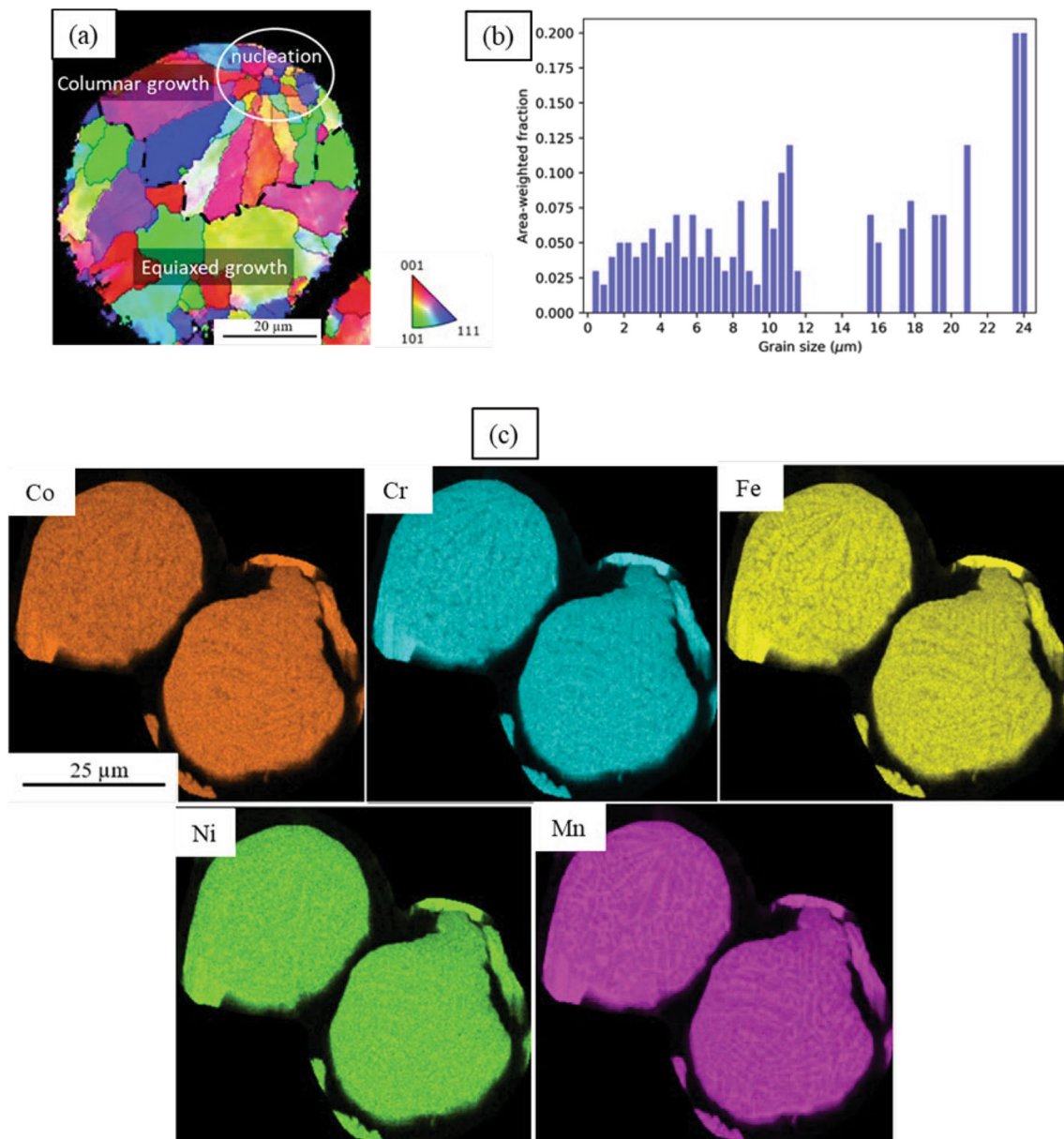


Fig. 4 EBSD IPF map (a) of a powder particle and the grain size distribution of about 15 powder particles analyzed (b). The short-dashed black lines in (a) were manually included to differentiate

between the columnar and equiaxed grain growth in the powder particle. (c) The EDS mapping of the powder microstructure

in addition to the effect of particle size-dependent impact energies on the deformation of the particles upon impact. The HEA splat flattening ratio in the SEM micrograph and numerical model was evaluated. The flattening ratio, defined as the ratio of the splat width to the splat height, can evaluate the extent of plastic deformation of the HEA particles during CS. The splat width and height were evaluated as the major and minor axes of the oblate spheroid splat shape (Ref 47) within the deposit microstructure. Fifteen splats with clear splat boundaries and different sizes were evaluated within the SEM micrograph of the deposit cross section and the numerical model.

Flattening ratios (average with standard error) of (2.0 ± 0.2) and (1.9 ± 0.1) were obtained in the deposit microstructure and numerical model, respectively. Again, these values indicate that the FEA model predicts the HEA particle deformation behavior during cold spraying well. These values can be inevitably associated with errors as mechanically polished cross sections do not usually pass through the center of splats. In addition, actual cold spray parameters such as particle impact and substrate temperature, actual mechanical properties of the powder material, and the limitations of the numerical approach would likely influence the flattening ratio calculations. Nevertheless,

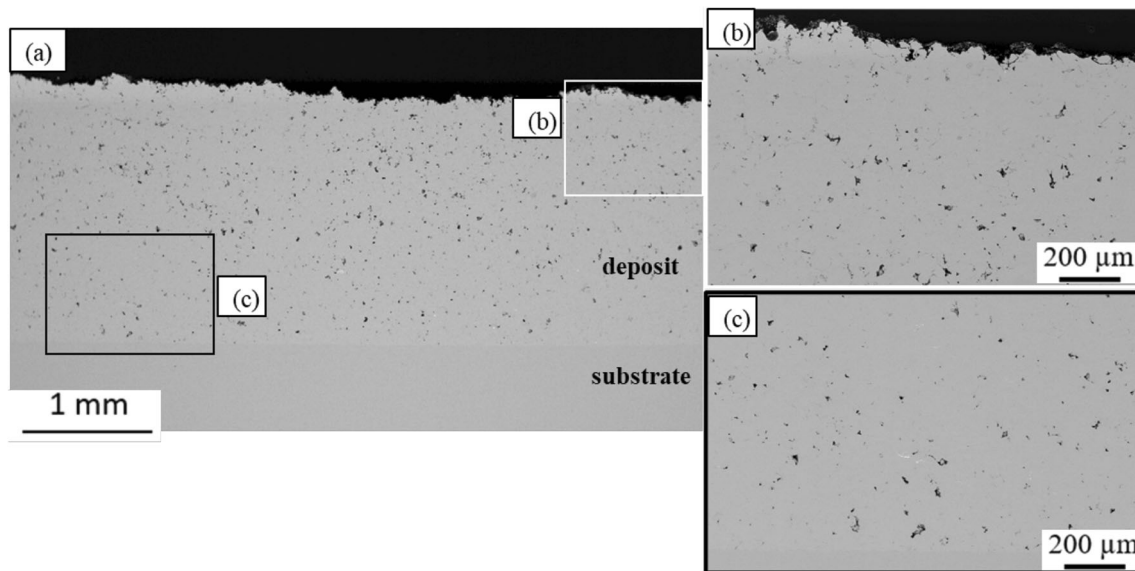


Fig. 5 Low-magnification BSE SEM micrograph of the cold-sprayed CoCrFeNiMn HEA deposit on the substrate (a). High-magnification images of the deposit's top and bottom layers are shown in (b) and

(c). The high-magnification SEM micrographs were taken from the region indicated with a square box in (a)

this approach has been employed in previous work (Ref 32, 48), giving an approximation of the flattening ratio and, subsequently, the plastic deformation morphology of the particles.

As cold-sprayed deposits are composed of many splats, their mechanical properties, such as elastic modulus and hardness, can be influenced by inter-splat bonding. The high-resolution BSE micrograph of the deposit closer to the deposit–substrate interface shown in Fig. 6(b) (magnified view of Fig. 6a) allowed a closer look at splat boundaries. The figure shows clear boundaries and gaps between splats (the coloring was done using the ImageJ software). The clear splat boundaries within the deposit likely suggest poor bonding between the HEA particles during cold spraying. Also, “textured” and “smooth” regions are generally observed at splat interiors and impact interface vicinity in the BSE micrograph, respectively. The smooth regions are likely the diffraction of high dislocation densities and the large number of grain boundaries at the impact regions, whereas the projection from the textured regions suggests lower dislocation densities and grain boundaries within splats.

Deposit Microstructures

XRD Profile

The XRD profile for the HEA powder and cold-sprayed deposit is provided in Fig. 7. The powder and cold-sprayed deposit exhibited an FCC structure (PDF-00-065-0528). As expected, the feedstock powder FCC structure was retained

in the cold-sprayed HEA deposits with no other phases detected by the used XRD analysis. The XRD profile of the cold-sprayed deposit showed peak broadening, indicating the presence of subgrains and residual strain formed during the severe plastic deformation of the HEA.

EBSD Characterization: Close to the Deposit–Substrate Interface

A high-magnification EBSD and high-resolution SEM micrograph of the deposit–substrate interface is presented in Fig. 8. This was acquired to investigate the microstructural characteristics of the interface between the cold-sprayed HEA particle–substrate that resulted from the impact-induced severe plastic deformation during cold spraying. Figure 8(a) and (b) presents the SEM and band contrast micrographs. The band contrast shows the quality of the backscattered signal reflecting the degree of lattice distortion. In particular, regions of intense plastic deformation, such as grain boundaries containing lattice defects, correspond to the dark lines. Randomly oriented dark lines, usually corresponding to the presence of a network of dislocations, were seen in the vicinity of the deformed particle–substrate interface, suggesting severe plastic deformation mainly limited to the interface vicinity, which agrees with previous studies (Ref 15, 16). A closer view in the band contrast image reveals elongated, linear dark lines parallel to the impact direction present away from the splat vicinity toward the interior. These linear features also appear to be parallel to the impact direction suggesting features similar to substructural deformation features such

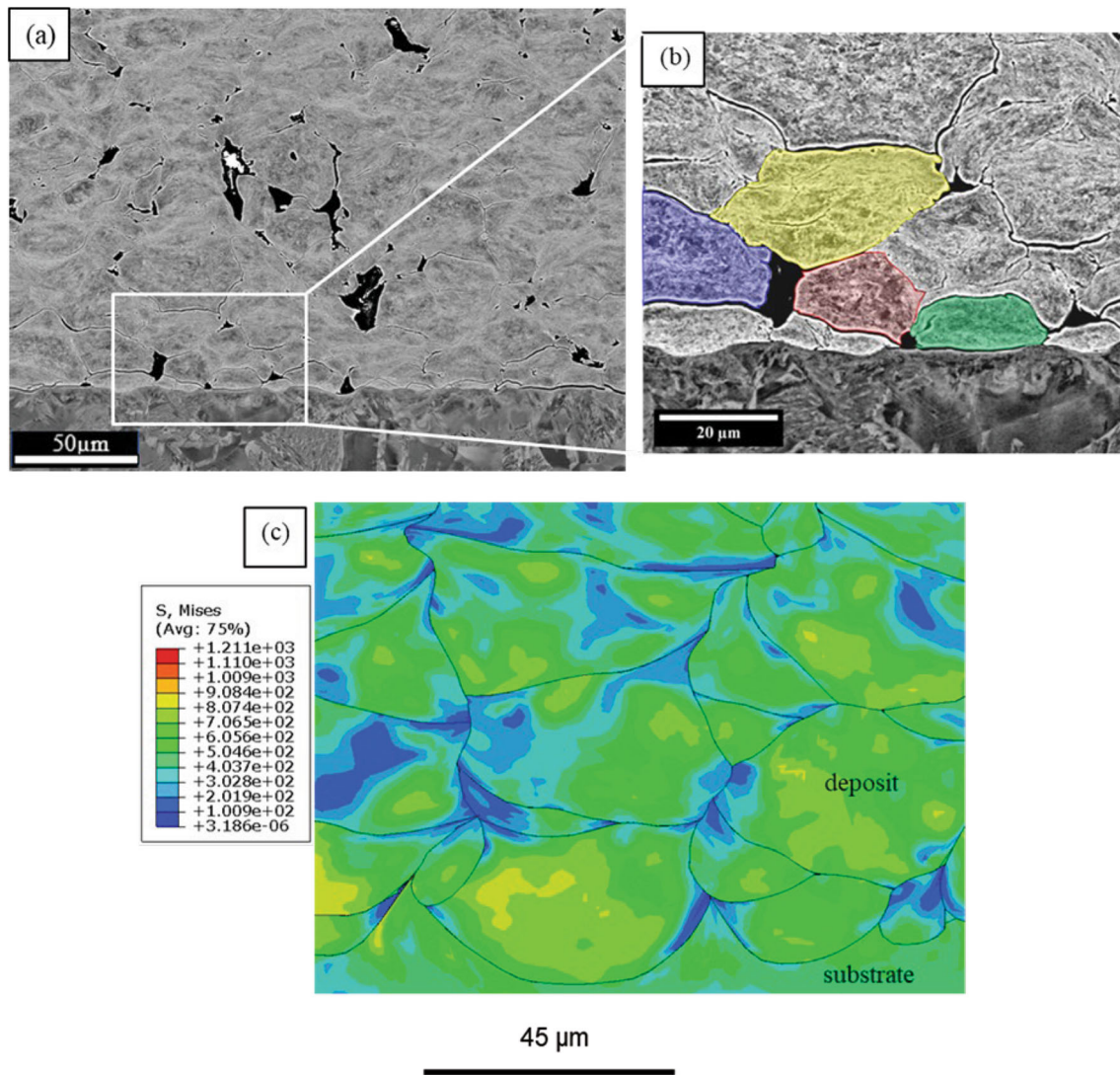


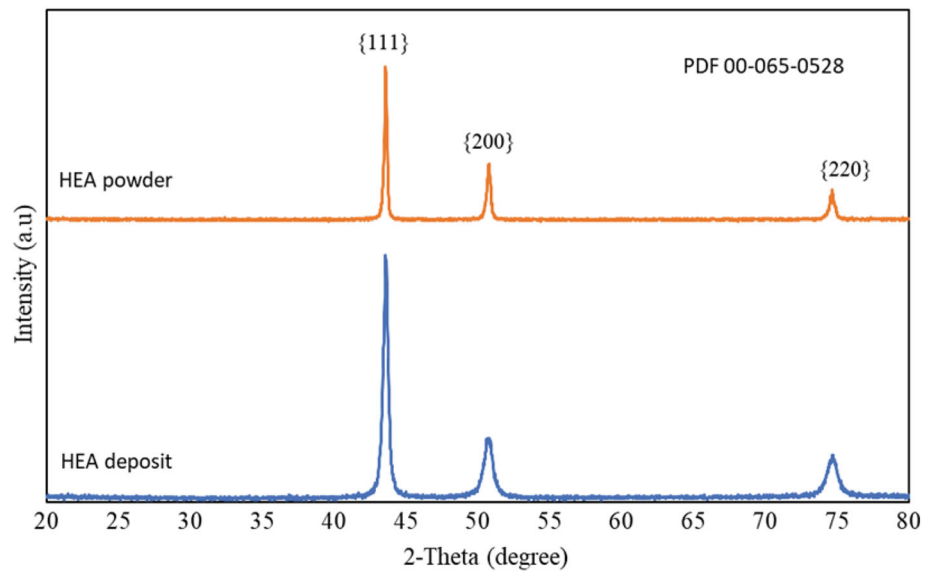
Fig. 6 (a) A high-contrast BSE micrograph of the cold-sprayed HEA deposit. A closer look at the interface and inter-splat boundaries is seen in the magnified view in (b). Similar deformation morphology of

the particles is observed in the SEM micrographs and the multi-particle FEA deformation simulation (c)

as twinning. Previous studies have reported similar deformation features. For instance, cold-sprayed CoCrFeNiMn HEA (Ref 18, 19, 49) and dynamic and static deformation of bulk CoCrFeNiMn HEA (Ref 5, 6, 50); however, these deformation features require further investigation as detailed characterization of the feature may be difficult with the technique employed. Furthermore, Fig. 8(c) and (d) shows the IPF and kernel average misorientation (KAM) maps of the particle–substrate interface. The figures reveal coarse grains at regions away from the interface of the particle and substrate, and fine grains at the interface. The dark regions at the interface are a result of poor diffraction quality or indexation. The regions likely contain refined grains with sizes below the resolution or step size of the EBSD analysis (50 nm) and high density of dislocation as revealed by the band contrast in Fig. 8(b), hence the poor

diffraction or indexation quality. Away from the interface, toward the center of the particle, are elongated subgrains, likely deformed in the shear or compression direction. Using a color gradient (threshold between 0 and 5), the KAM map illustrates localized strain variations within the microstructure. Blue corresponds to the absence of misorientation, while green or yellow indicates a high misorientation. Higher KAM reflects denser GNDs. Higher local misorientations are concentrated at the interface, and away from the interface, the KAM value decreases to strain-free regions (showing mainly blue colors). The high misorientation indicates localized strain and a high density of dislocations. Figure 8(d) and (e) shows the misorientation angle distribution of the region analyzed, and the misorientation angle distribution for below 5°. The misorientation angle distribution suggests grains with low-

Fig. 7 XRD profile of powder feedstock material and deposit, showing that the cold spray process did not result in phase transformation of the spray powder. There is peak broadening observed in the XRD profile of the deposit, likely resulting from the plastic deformation during cold spraying



angle grain boundaries (LAGBs $< 15^\circ$) and high-angle grain boundaries (HAGBs $> 15^\circ$) and boundaries with 60° misorientations. The KAM values reveal most misorientations are below 1.5° suggesting a deformation process—dynamic recrystallization, was dominant mainly at the particle–substrate interface.

To further gain more insight into the particle–substrate and particle–particle interfaces at the deposit–substrate interface, the microstructure of a region at the deposit–substrate interface was characterized using the EBSD technique. Figure 9 presents the microstructure micrographs of a region at the deposit–substrate with the indicated interface (Fig. 9a). The micrographs reveal a similar microstructure observed for the particle–substrate in Fig. 8. The IPF-Z map in Fig. 9(b) shows a varied mix of colors indicating randomly oriented grains in the deformed particle without any preferential orientation. Grain boundaries were detected when the misorientation was above 5° , with a minimum of 2 pixels per grain and a kernel size of 3×3 . The cold-sprayed HEA deposit–substrate interface is characterized by a bimodal grain-sized microstructure with randomly oriented fined grains that are dominant at the impact boundaries and larger grains at the interior of the splat. Also, the interface between particles is characterized by ultrafine grains, as these regions are poorly indexed resulting from the high strain and ultrafine grains with sizes likely below the resolution or step size of the EBSD technique employed (50 nm). Again, elongated subgrains are observed toward the interface, likely deformed in the direction of shear or compression. Furthermore, the KAM map shown in Fig. 9(c) reveals a higher local misorientation at the impact boundaries. The dark areas at the impact boundaries result from the low indexation quality due to severe plastic deformation of the region, as explained

earlier. Grains characterized with low strain (and a few strain-free areas mostly within grains) are observed in the interior of the splats (with blue color indicative of low or no strain or dislocation density). Also, Fig. 9(d) shows the plot of the KAM distribution of the deposit with most values below 1.5° , indicative of dynamic recrystallization mainly occurring at the impact interfaces. Referring to Fig. 9(e), the deposit microstructure likely consists of a mixture of LAGBs ($< 2^\circ$ to 15°) and HAGBs ($> 15^\circ$), and a fraction of grain boundaries that are $\Sigma 3$ $\{111\}$ 60° misorientation, which is characteristic of $\{111\}$ $\langle 112 \rangle$ deformation twinning in FCC metals (Ref 51).

To provide a more accurate picture of the LAGB and HAGB distribution across the impact interfaces and within a particle, the point-to-point and point-to-origin (cumulative) misorientation lines versus distance are plotted, as shown in Fig. 10. Figure 10(a) shows the IPF map from Fig. 9(b) where the misorientation lines or plot were taken from. The misorientation profiles from each line, as labeled, are plotted in Fig. 10(b). Three distinct regions were selected for the misorientation profiles—the central region of the particle (labeled (i)), particle–substrate interface (labeled as (ii)), and the particle–particle interface (labeled as (iii)). In the central region of the particle, there are only a small number of LAGBs mainly within the coarse grains. There are two peaks on the point-to-point misorientation profile with high misorientation angles, which is likely the angle of the grain boundaries within the distance analysed, as shown in Fig. 10(a). This suggests that subgrains were not well formed at the particle interior, indicating low local strain and dislocation density. Interestingly, in the impact regions; the particle–substrate and particle–particle interfaces, the ultrafine equiaxed grains appear to be highly misoriented, with the point-to-point

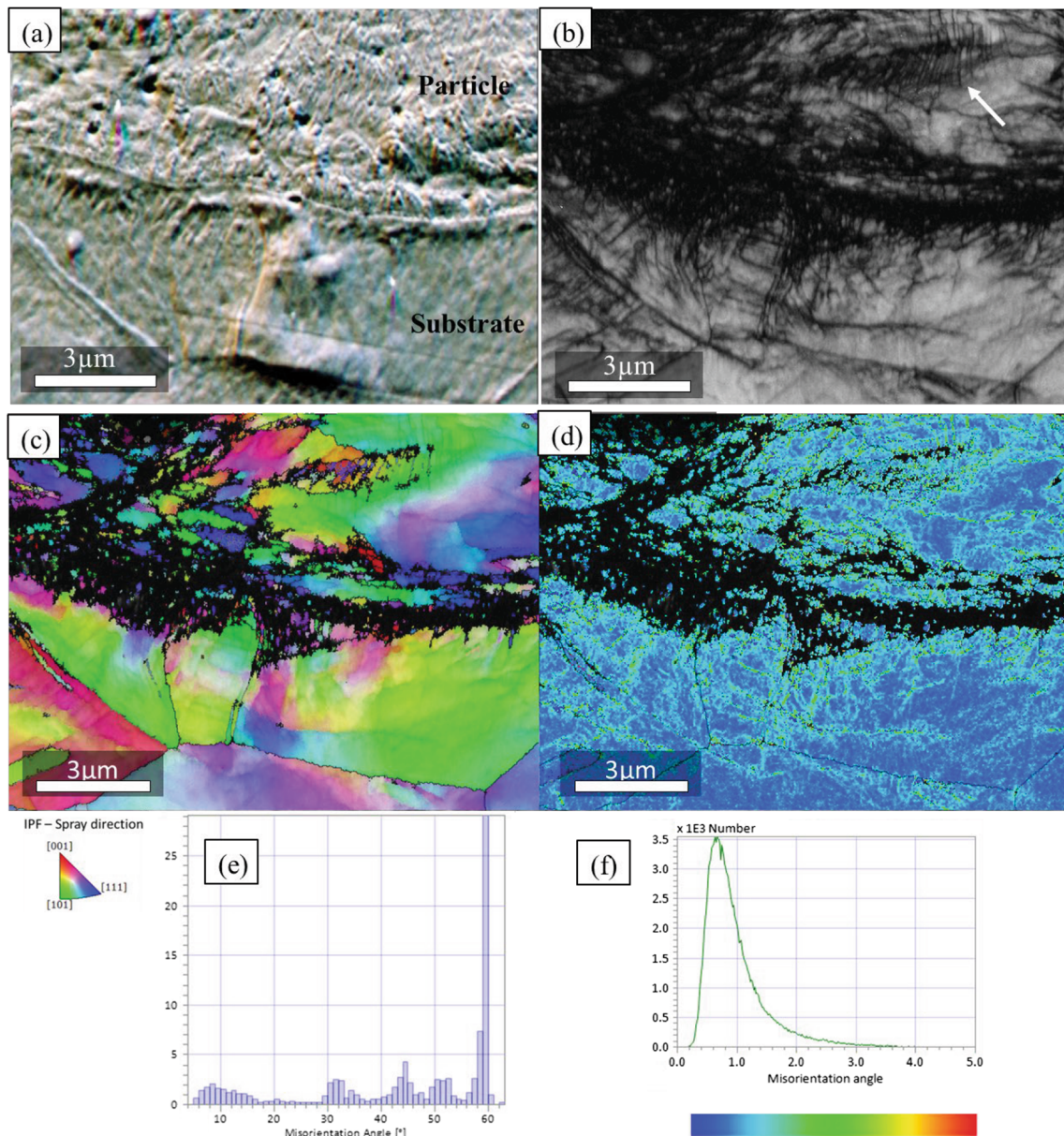


Fig. 8 A high-magnification, high-contrast BSE image (a) and EBSD band contrast image (b) of a cold-sprayed CoCrFeNiMn HEA particle at the deposit–substrate interface. A network of dislocations is observed at the interfaces, and likely substructure deformation features indicated by

the white arrow close to the particle interior, likely deformation twins. (c) shows the IPF map of the region analyzed and (d) the KAM map. The misorientation angle distribution and KAM distribution of the region analysed are presented in (e) and (f), respectively

misorientation reaching 40 and 60°. Although these regions are poorly indexed, HAGBs were likely formed at the bonding or impact regions.

From the EBSD results shown in Fig. 8, 9, and 10, it is apparent that distinct regions or microstructures can be identified, namely, the central particle region (Fig. 10a and b(i)), with less deformed coarse grains (Fig. 10a), and ultrafine grain region (Fig. 10a and, b (ii) and (iii)) at the impact interfaces. For these regions (i.e., the central region of the deposited particle, impact interfaces between particle–substrate and particle–particle), the strain and

temperature profiles versus distance at the end of the deposition were estimated from the FEA, shown in Fig. 11. Figure 11(a) shows an enlarged view of the multi-particle FEA deposit–substrate interface and regions where the line profiles were taken from. The strain and temperature profile from each line is plotted as labeled in Fig. 11(b). The central region of the deformed particle (labeled as (i)) reveals low strain and temperature value, with an average strain of 0.45 (45%) and temperature of 650 K from the center toward the south pole of the particle interior. At the particle–substrate interface region, there is a remarkable

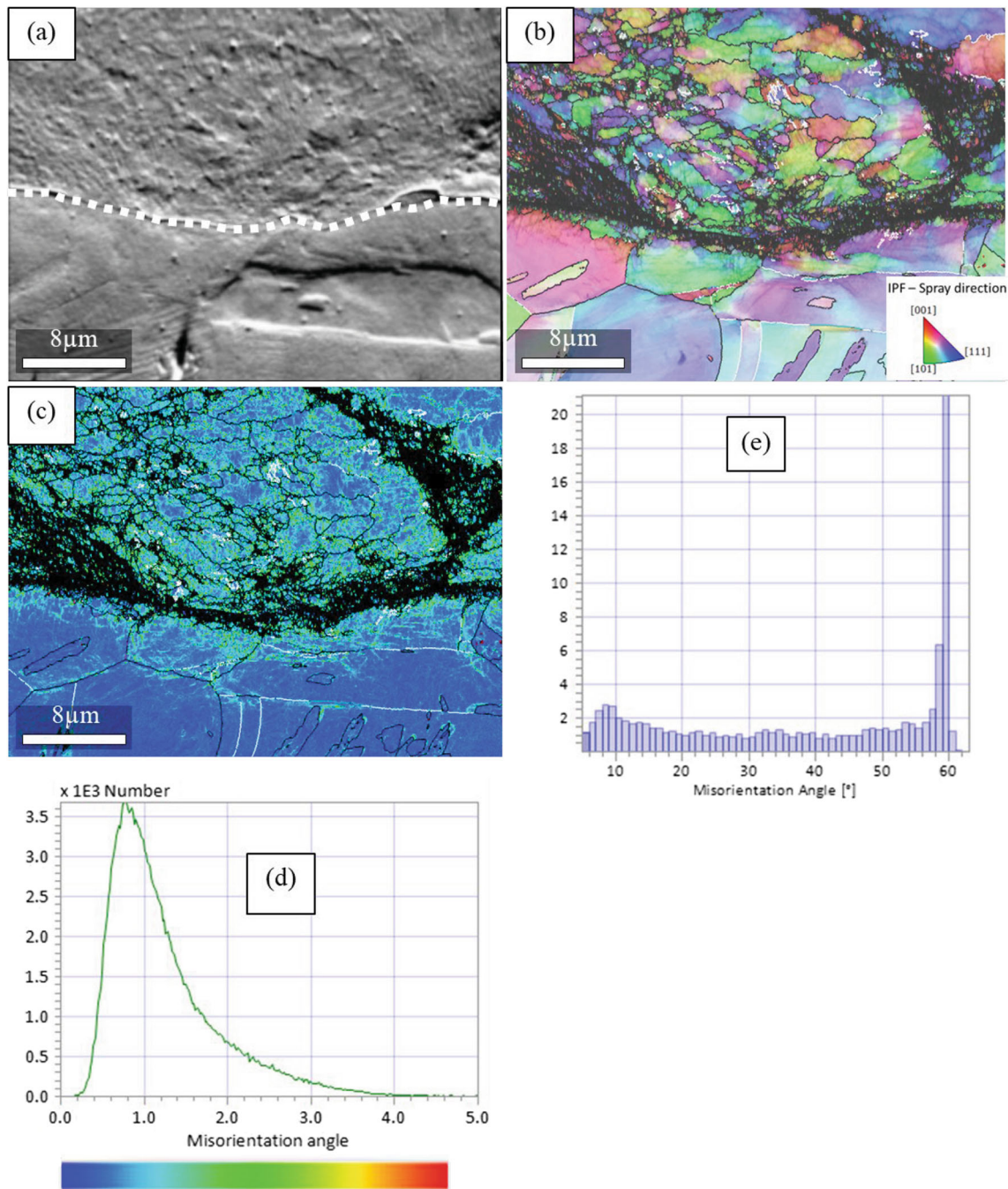


Fig. 9 The (a) BSE image, (b) EBSD IPF map, (c) KAM map, (d) KAM distribution of c, and misorientation angle distribution (e) of cold-sprayed CoCrFeNiMn HEA particle at the deposit–substrate interface

increase in strain and temperature, with strain and temperature reaching 4.5 (450%) and 1310 K, respectively, at the interface. Similarly, the strain and temperature profile at the particle–particle interface region reaches their highest peak values at the interface. The remarkable increase in the deformation field variables at the interface likely contributed to the difference in the misorientation angles relative to the central region of the particle, as shown in Fig. 10, which also correlates with the ultrafine

equiaxed grains observed at the impact interfaces in Fig. 8 and 9.

EBSD Characterization: Within the Deposit

The EBSD analysis of the deposit–substrate interface shown in Fig. 8 and 9 reveals a heterogeneous microstructure formed, with ultrafine grains at the impact interface while large grains are within the splats. To

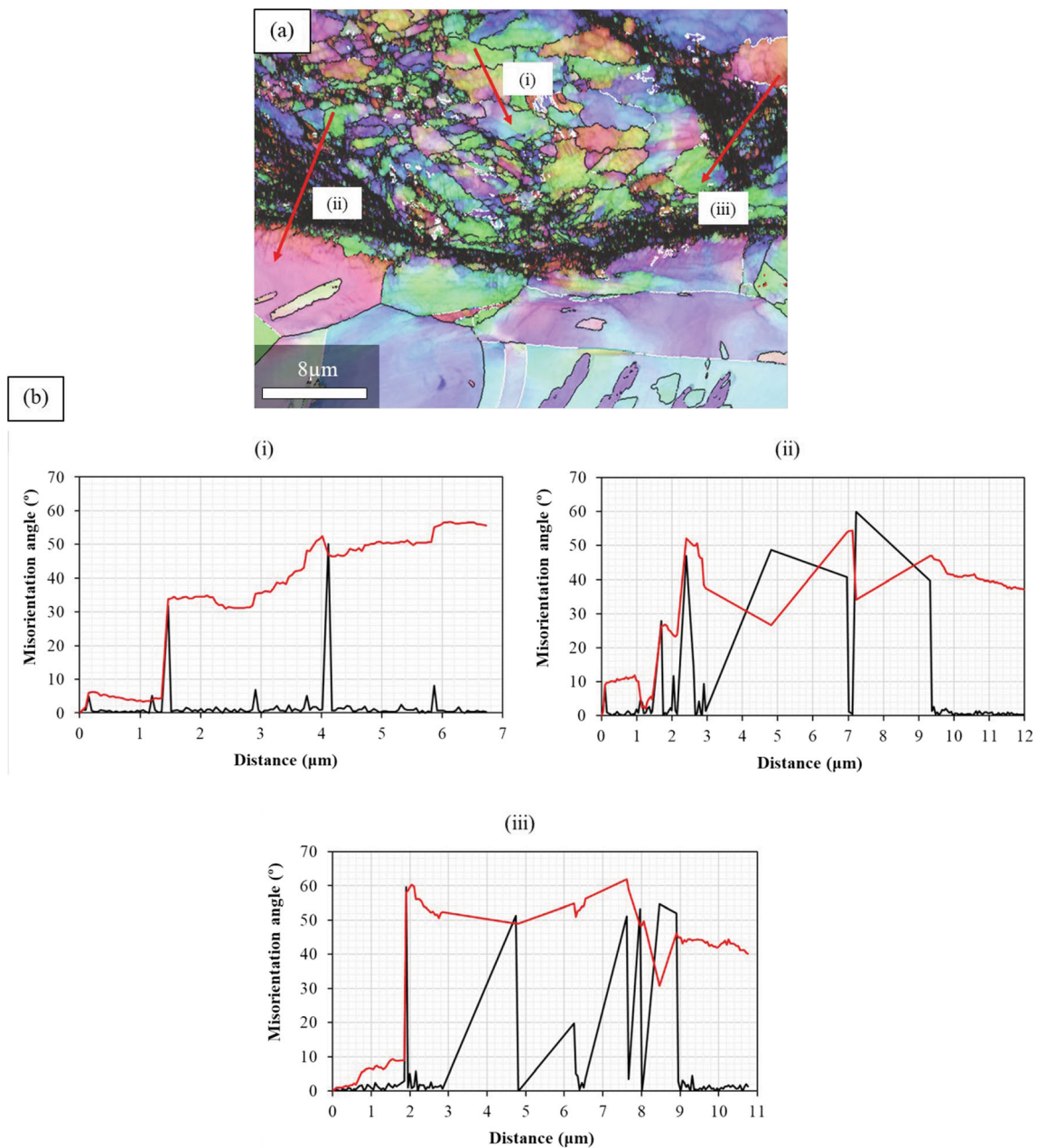


Fig. 10 (a) The IPF map in Fig 9b, with marked lines in different regions and their corresponding misorientation profiles (b). The misorientation profiles show the point-to-point (the black curve) and

point-to-origin (cumulative) (the red curve) along the distance analyzed (Color figure online)

confirm the same within the central region of the cold-sprayed HEA deposit, a lower magnification micrograph covering a wider area within the deposit was analyzed using the EBSD technique. Figure 12(a) and (b) shows high-contrast BSE and band contrast images of a region within the deposit. The micrographs reveal that the HEA particles had undergone extensive plastic deformation, mainly at the particle interfaces. Also, in Fig. 12(a), a micro-crack is observed, likely a gap at the inter-particle boundaries resulting from incomplete bonding, similar to

what is observed in Fig. 6(b). Furthermore, Fig. 12(c) shows grains colored according to the IPF in the impact direction. Equiaxed ultrafine grains are dominant at the impact interfaces. Also, elongated subgrains can be seen close to the interface, likely deformed in the direction of shear or compression, first upon impact and then by subsequent particle impacting. The orientation of the elongated subgrains likely depends on the orientation of the particle during deformation. Within the particles or splats are coarse elongated and equiaxed grains with sizes similar

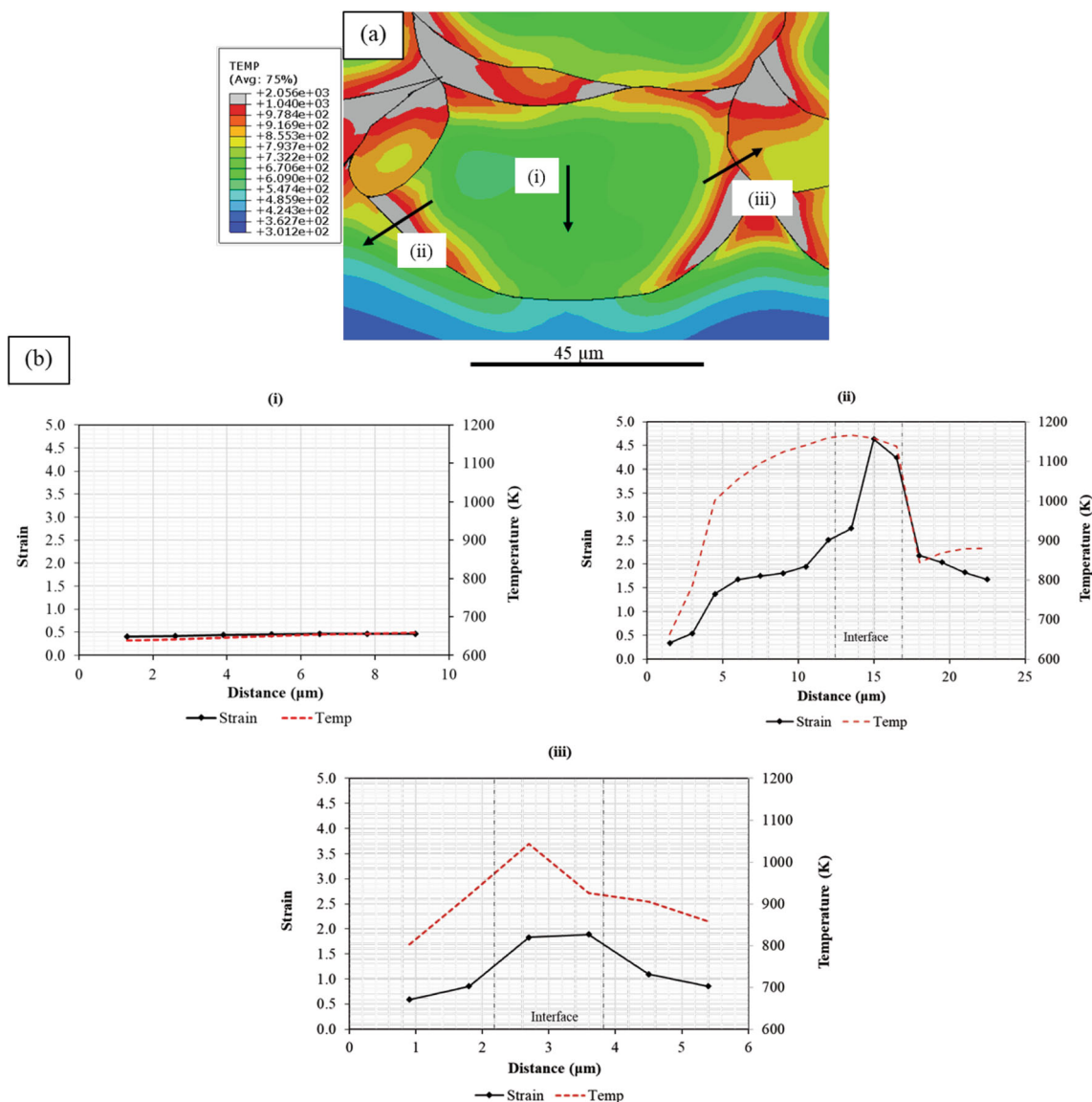


Fig. 11 (a) A close view of the temperature profile of a region in Fig 6c, of the FEA multi-particle impact model. The strain and temperature along the marked lines in (a) are presented in (b)

to the original feedstock powder shown in Fig. 4(a). Interestingly, the ultrafine grains surround the coarse grains within the splats or particles, as the coarse grains have likely experienced less deformation, thus resulting in a HEA deposit with a heterogeneous grain-sized microstructure. Grain size analysis of the deposit (3500 grains, at least 5 pixels per grain) revealed an area-weighted average grain size of $\sim 3.3 \mu\text{m}$, with most grains below $\sim 1 \mu\text{m}$, as shown in Fig. 12(d), confirming grain refinement when compared to the original feedstock powder. Figure 12(e), (f), and (g) presents the KAM map, dislocation density map, and misorientation angle distribution. The KAM and dislocation density maps (Fig. 12e and f) reveal that the splat interfaces have experienced severe plastic deformation, leading to the high local strain

and dislocation density— 10^{16} m^{-2} . Naeem et al. (Ref 52) reported a similar value for the dislocation density of the HEA; a peak value of $\sim 1 \times 10^{16} \text{ m}^{-2}$ was found at around 45% of tensile plastic deformation. The dislocation density did not increase beyond the peak value attributed to dislocation annihilation due to dynamic recovery. The white areas in Fig. 12(e) and (f) are poorly indexed locations due to severe plastic deformation of the regions. Again, as observed in the previous EBSD analysis (Fig. 8 and 9), the KAM value of the HEA deposit microstructure is below 1.5° , indicative of dynamic recrystallization during cold spraying of the HEA particles. The misorientation angle distribution (Fig. 12g) shows that a higher fraction of the grain boundaries is LAGBs, and $\Sigma 3 \{111\} 60^\circ$ misorientation—characteristic of deformation twinning

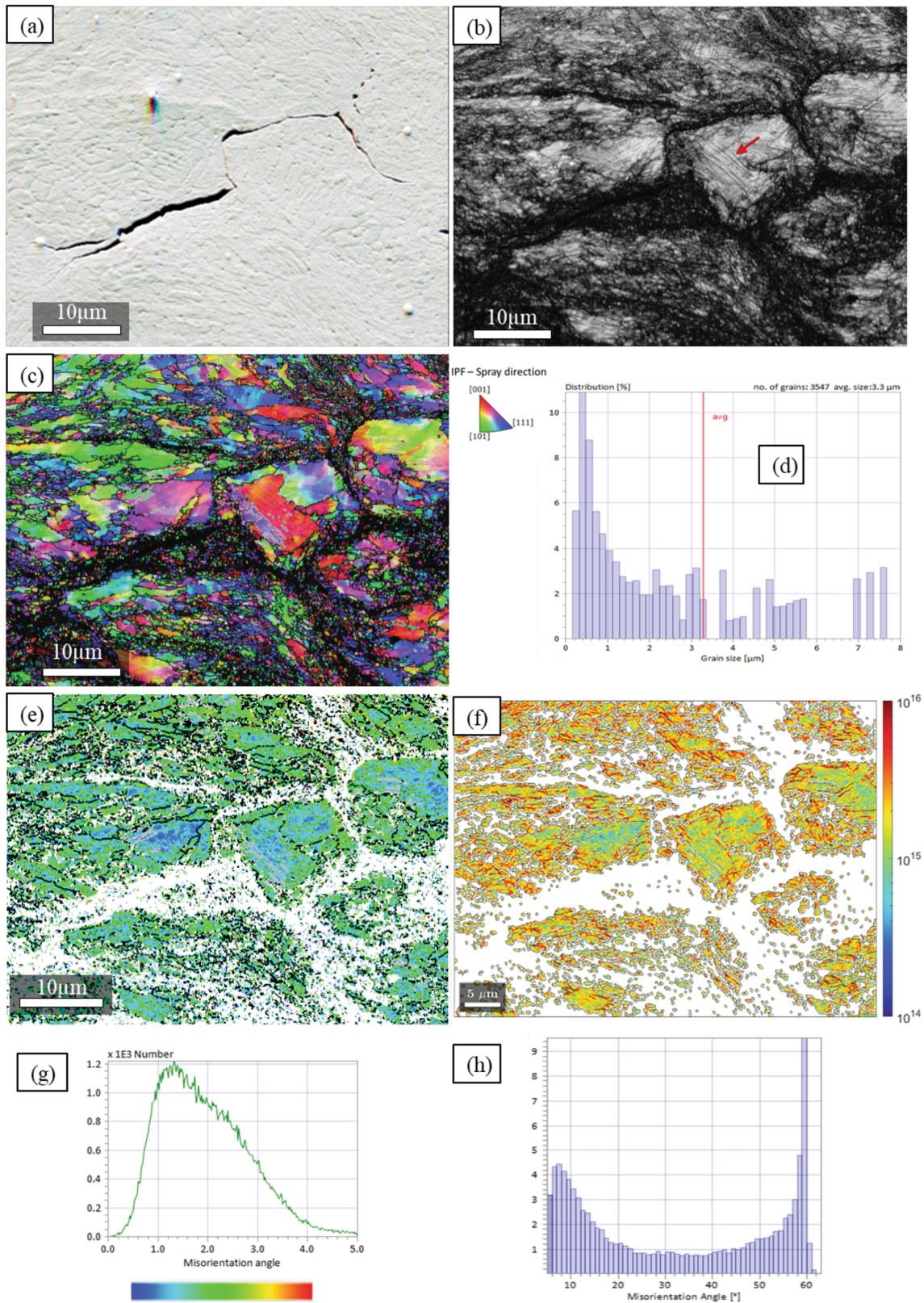


Fig. 12 The high-contrast BSE image (a), EBSD band contrast (b), EBSD IPF map (c), and grain size distribution (d) of the cold-sprayed CoCrFeNiMn HEA deposit microstructure. The red arrow shows substructure deformation features that are likely twins. KAM map (e),

dislocation density map (f), KAM distribution (g), and misorientation angle distribution (h) of the cold-sprayed HEA deposit microstructure are presented (Color figure online)

boundary, likely formed during the plastic deformation of the HEA material.

The FEA multi-particle simulation was analyzed to shed light on the particle dynamic recrystallization resulting from ASI—strain localization and strain-induced heating at the splats periphery. Figure 13(a) and (b) shows the results of the numerical simulations of strain and temperature profiles of subsequently impacted HEA particles on the substrate. It is seen that highly localized strain (> 2.5) and temperature (> 0.95 of the HEA solidus temperature) near the impacting interface were prominent due to thermal softening dominating over strain hardening during severe plastic deformation. The higher strain and temperature at the impact interface would result in thermally activated interfacial phenomena such as bonding, ASI and dynamic recrystallization (Ref 15, 27, 53). This is consistent with the indexing quality of the EBSD analysis—poorly indexed zones occur in regions with high plastic deformation, leading to significant lattice distortion and hence, poor diffraction.

From the EBSD micrographs shown in Fig. 12, smaller particles were observed to have interior grains with sizes close to those at the interface, whereas larger particles show a more heterogeneous microstructure with grains in the particle interiors larger than those at the interfaces. The possibility of this phenomenon during cold spraying of the HEA was investigated using the FEA model. Strain and temperature analyses were performed at the center of splats from the FEA model. To evaluate the effect of particle size on the severity of deformation and grain refinement at the interior of the splats during cold spraying, five small and five large particles of sizes 10–25 μm (below the experimental mean particle size) and 30–45 μm (above the experimental mean particle size), respectively, were evaluated. The average temperature and strain evolution of the different particle size ranges is presented in Fig. 13(c) and (d). The average maximum temperature of 815 K obtained within smaller particles resulting from strain-induced heating could favor the dynamic recrystallization of grains within the particles. This means that grains within smaller particles likely experienced more grain fragmentation when compared to those of larger particles (having an average maximum temperature of about 675 K). These analyses suggest that larger particle sizes would likely achieve a higher fraction of elongated coarse grains, but with the smaller particles achieving a higher fraction of ultrafine grains—both contributed to the heterogeneous microstructure.

Nanohardness

Nanohardness was measured on the mirror-polished HEA powder and deposit cross sections. An average

nanohardness value of 1.16 ± 0.49 GPa was measured on the powder particles. Figure 14(a) shows an SEM micrograph of the array of indents (the array shape displayed is due to avoiding regions of large pores during the nano-indentation testing) with the indents denoted at particle central regions and impact interfaces. The denoted indents were analyzed to provide information on the effect of the cold-sprayed HEA heterogeneous microstructure on the nanohardness variation. Figure 14(b) shows the nanohardness values of each indent, as denoted in the SEM image. Indents were taken from regions with clear interfaces from the SEM image. The corresponding nanohardness distribution histogram is provided in Fig. 14(c). It is seen from the scatter plot in Fig. 14(b) that the indents at the impact regions result in greater nanohardness measured when compared with those at the splat interior or central region. For the nanohardness analyzed in those regions, it was found that the average nanohardness at the impact region is (0.65 ± 0.04) GPa greater than the average nanohardness at the central region of the particles. Moreover, the nanohardness values at the impact region analyzed varied from 4.77 to 6.30 GPa; meanwhile, at the central region they varied from 4.29 to 4.97 GPa. Moreover, the nanohardness distribution histogram presented in Fig. 14(c) suggests heterogeneous variation in the nanohardness values measured within the cold-sprayed HEA deposit. An overall average nanohardness and Young's modulus values of (5.14 ± 0.08) GPa and (194 ± 1.64) GPa, respectively, were obtained for the deposit. A similar nanohardness value has been reported by Feng et al. (Ref 20) for cold-sprayed CoCrFeNiMn deposit (5.64 GPa). The nanohardness value measured for the cold-sprayed HEA deposit is higher than the conventional as-cast HEA with a hardness value of 4.13 GPa, attributed to the high density of dislocations and grain boundaries resulting from the severe plastic deformation of the HEA particle during deposition, as mentioned in Section 3.3.

Microhardness

Microhardness was measured on the cold-sprayed HEA deposit cross section, with an average value of (280 ± 3.59) $\text{HV}_{0.3}$. The distribution of the microhardness value measured for the HEA deposit is shown in Fig. 15(a), ranging from 118.97 to 490.21 $\text{HV}_{0.3}$. Figure 15(b) shows the average microhardness value measured from close to the top of the deposit to the substrate. There are negligible variations in the measured microhardness value within the deposit, indicating likely uniform plastic deformation throughout the deposition, layer by layer. The cold-sprayed deposit in this study revealed a relatively higher measured microhardness value than conventional additively manufactured (Ref 54, 55)—160 to 212 HV and as-cast

Fig. 13 The finite element simulation contour plots of strain (a) and temperature (b) localization of the multi-particle impact of the CoCrFeNiMn HEA. Higher strain (> 2.5) and temperature ($> 0.65T_{melt}$) are observed at the particle interfaces. Plots of strain (c) and temperature (d) of small and large particles (10 particles in all with a size range of 10–25 μm for small particles and 30–45 μm for large particles, mainly at the center of the FEA model)

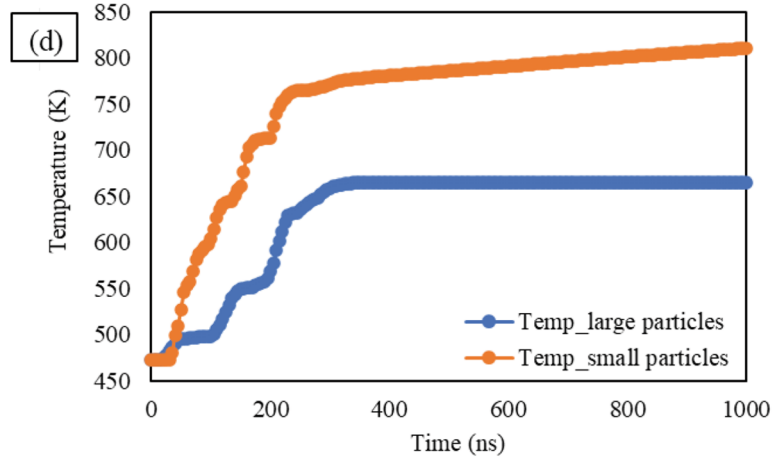
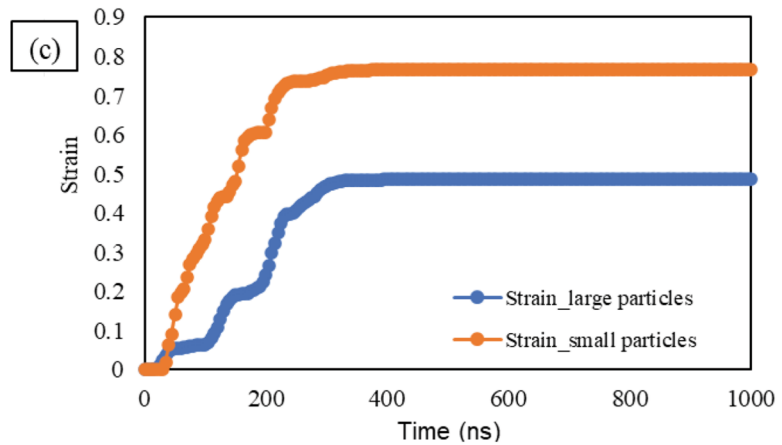
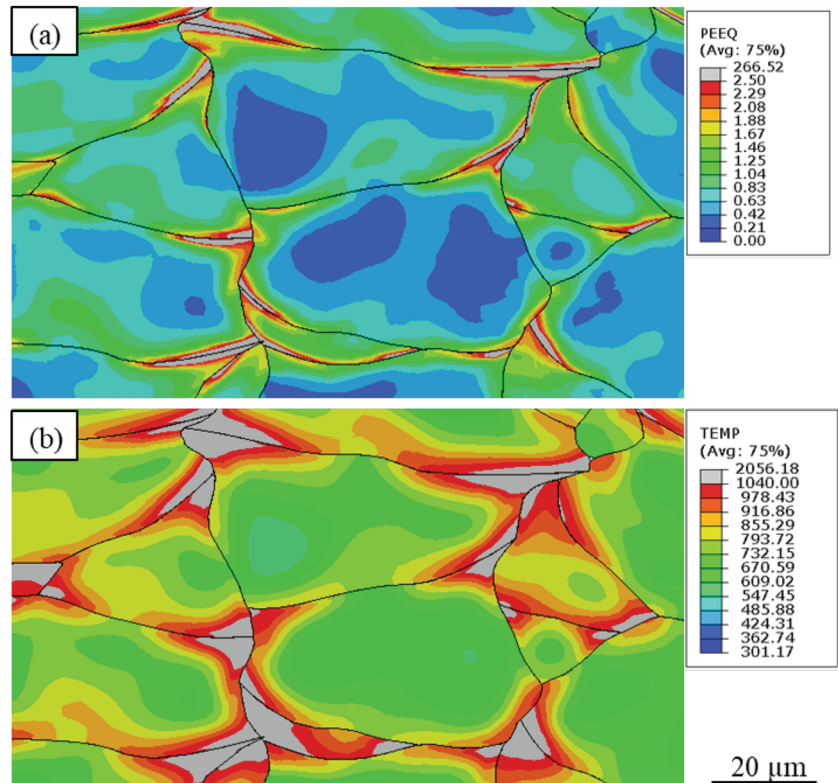


Fig. 14 SEM micrograph showing an array of nano-indentations (a), (b) the plot of the average nanohardness values of the regions denoted and labeled in (a), and (c) the corresponding nanohardness distribution of the cold-sprayed HEA deposit (b)

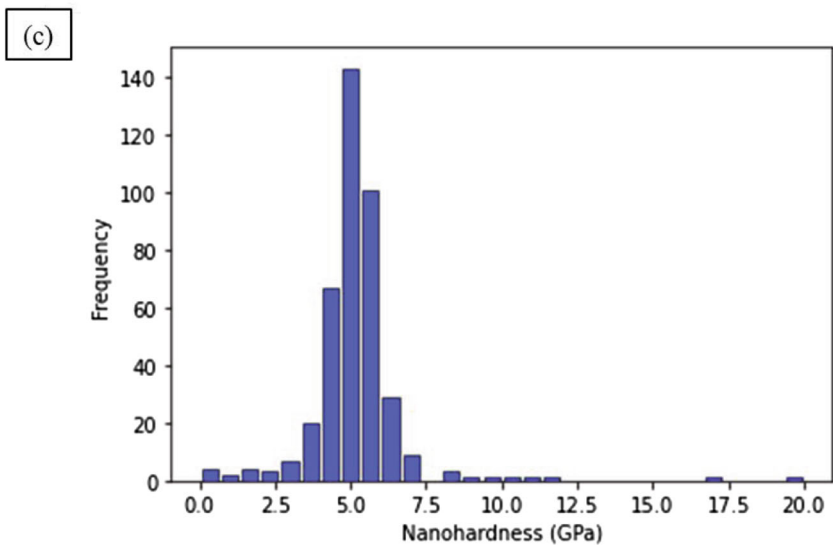
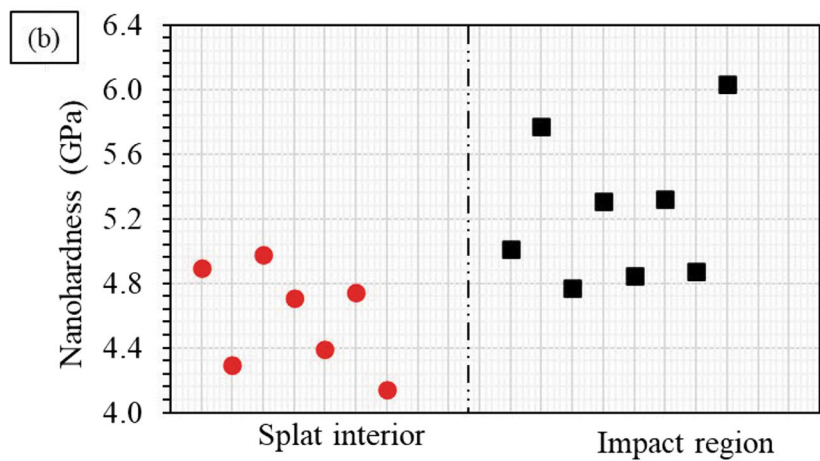
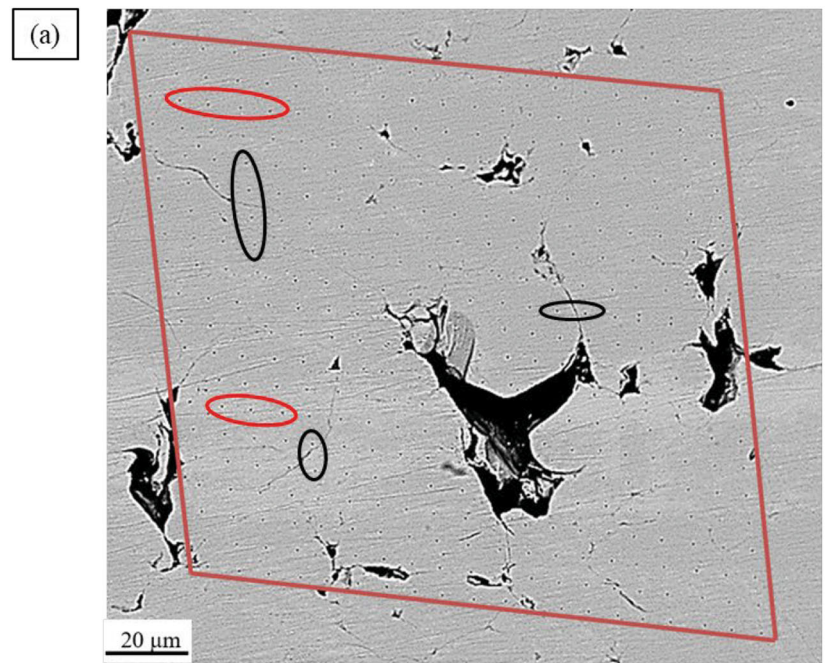
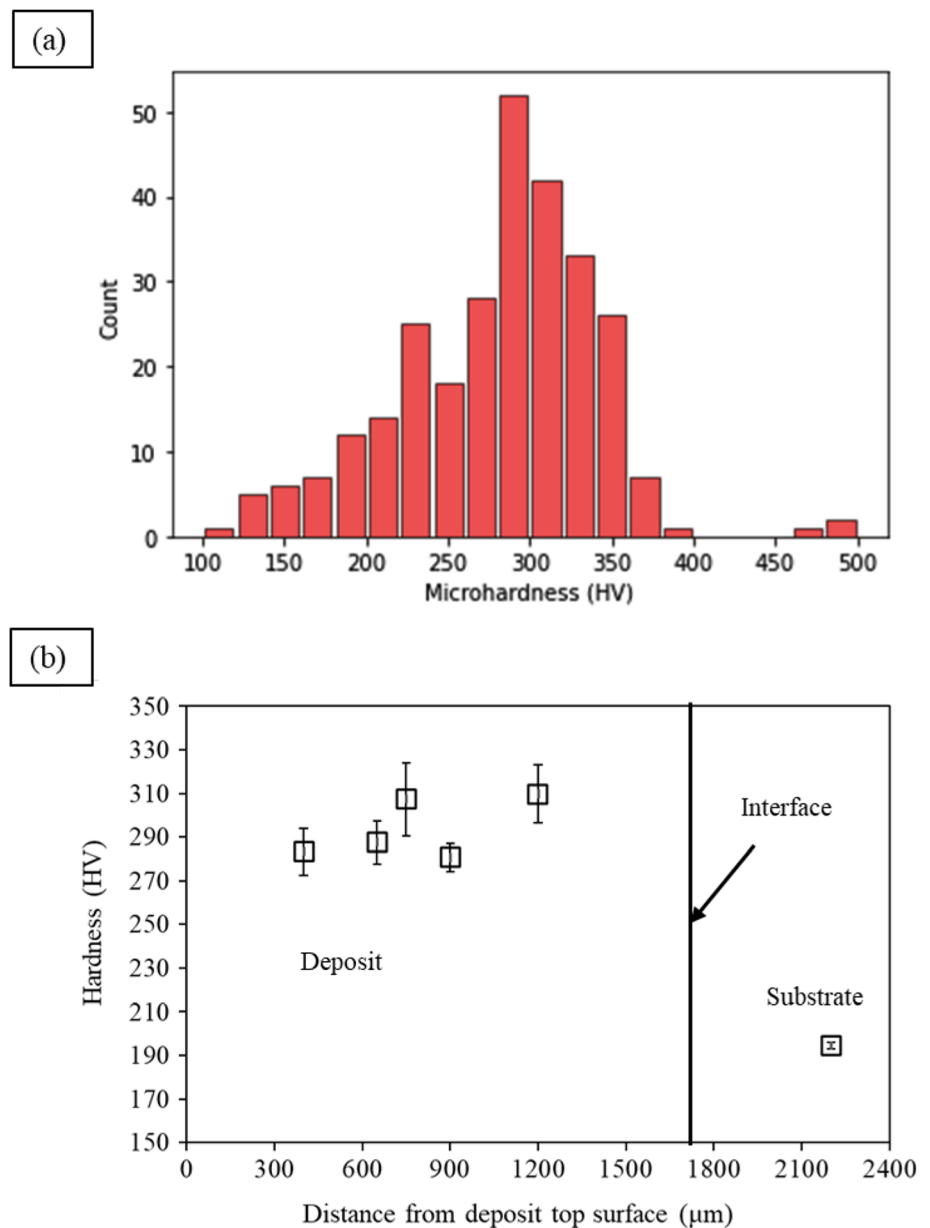


Fig. 15 The distribution of the microhardness value measured for the cold-sprayed HEA deposit (a), through-thickness hardness variations of the deposit from the deposit top (about 300 μm) to the substrate (b)



CoCrFeNiMn HEA (Ref 49)—144 HV. This is attributed to the severe work hardening and grain refinement during cold spraying of the HEA.

Discussion

The moderate porosity ($\sim 2.4\%$) and inter-splat boundaries observed in the cold-sprayed HEA deposit, shown in Fig. 6(b) and 12(a), are consistent with the high strain hardenability and resistance to shear localization of the HEA (Ref 56). The poor inter-particle bonding suggests insufficient thermal softening and deformation for complete metallurgical bonding of the HEA particles during

cold spraying. Higher particle velocities or gas temperature can reduce the microstructural defects in the cold-sprayed HEA deposit but at the expense of cost. Since the cold spray equipment was operated at the upper limits of pressure and temperature, achieving a pore-free deposit may not be possible due to the HEA impact behavior, as observed in a previous study by Nikbakht et al. (Ref 18). Another plausible explanation for this deformation behavior is likely a small, well-bonded area at the particle–particle interfaces and a high thermal gradient (as observed in Fig. 13) within the particles. The outcome of these impact phenomena or deformation behavior would likely result in the rupture of the splats' bond during the elastic unloading

of the splats (Ref 57) and hence the clear inter-particle boundaries.

Most notably, based on the evidence obtained from the EBSD analysis in Section 3.3, the overall deformation appears to result in heterogeneous microstructures formed in the cold-sprayed HEA deposit. The severe plastic deformation of the HEA particles resulted in, elongated subgrains formed close to the impact interfaces, and equiaxed ultrafine grains formed at the impact interfaces, whereas coarse grains were observed at the central region of the particles (Fig. 8, 9, and 12). The large deformation at extremely high strain and strain rates during the cold spraying process can dramatically result in grain refinement via ASI and dynamic recrystallization, mainly at splat impact boundaries, and severe work hardening effects. Moreover, the dislocations formed and grain refinement during the impact-induced plastic deformation likely result in residual lattice microstrain, leading to the peak broadening in the XRD patterns shown in Fig. 7.

The combined study of the EBSD characterization and FEA shed light on the bonding mechanism and grain structure resulting from the thermomechanical phenomena—dynamic recrystallization and ASI. The misorientation profiles and the FEA strain and temperature profiles in Fig. 10, 11, and 13(a) and (b) reveal the mechanisms for bonding and formation of the heterogeneous microstructure of the cold-sprayed HEA. The results reveal that during particle impact, the previously coarse grains likely experienced a dramatic increase in dislocation density, which accumulate and rearrange into LAGBs forming subgrains. As deformation-induced strain and temperature increase during the deformation process, particularly the remarkable increase at the impact or bonding regions, the subgrains rotate and their misorientation angle increases to accommodate the increasing strain, leading to the formation of HAGBs and randomly oriented ultrafine grains. The elongated grains formed close to the interface can be due to the accumulation and alignment of many dislocations in a short time. Similar deformation mechanisms and the resulting microstructural features have been reported for cold-sprayed Ni particles (Ref 15), the CoCrFeNiMn HEA (Ref 18, 58) and high strain rate deformation of bulk stainless steel material (Ref 59). This strain-induced increase of grain boundary misorientation via rotation of subgrains within the short time of deformation is representative of continuous dynamic recrystallization (Ref 15), which is believed to be the dominant mechanism for grain refinement in the cold-sprayed HEA deposit. The schematic illustration in Fig. 16 explains the formation of the ultrafine grains at the impact interfaces by rotational dynamic recrystallization. Moreover, Assadi et al (Ref 27) suggested that the bonding of particles during cold spraying is attributed to ASI, due to localized strain and temperature at

the bonding regions, as shown in Fig. 11. Therefore, rotational dynamic recrystallization and ASI are likely the mechanism of bonding and formation of highly misoriented ultrafine grains at the bonding regions between the HEA particles and particle–substrate.

Similar microstructural evolution was observed within the cold-sprayed deposit as shown in the EBSD micrographs in Fig. 12. The figure reveals equiaxed ultrafine grains formed at the bonding or impact regions, whereas coarse grains were observed at the central regions of the particles. Moreover, one can see from the KAM map shown in Fig. 12(d) that a high density of dislocations was accumulated at the impact interfaces, indicating localized high strain at the impact or bonding region. The higher misorientation or local strain at the splat or impact boundaries can be due to the localized and intense deformation field variables, including temperature, strain, and strain rate, as explained earlier. Since measuring the plastic strain at the impact interfaces is not yet experimentally feasible, using FEA tools for the multi-particle impact deformation (shown in Fig. 11 and 13) gave an idea of the strain and temperature-induced. From the FEA impact modeling, a very high strain of more than 250% is found at the impact interfaces, with the temperature reaching over 90% of the alloy solidus temperature (Fig. 10 and 13a and b). This induced high strain and temperature via severe plastic deformation result in thermal softening and grain refinement near the particle–particle and between the particle–substrate interface where ASI dominates. The deformation mechanism via dynamic recrystallization and ASI explained for the particle–substrate and particle–particle interfaces at the deposit–substrate regions (Fig. 10 and 11) simply applies within the deposit. Also, elongated grains were observed to be formed close to the particle–particle interfaces, as shown in Fig 12(c).

Additional microstructure features observed in Fig. 8 are believed to possess boundaries with $\Sigma 3 \{111\} 60^\circ$ misorientation (from misorientation angle distribution presented in Fig. 12h) characteristic of deformation twinning. Moreover, the features appear parallel to the impact direction, confirming that these features were likely formed during the HEA particle deformation. Previous research has reported intensive deformation twinning and grain refinement to be the two main features of microstructure evolution in the HEA processed via HPT (Ref 11). Similar features have been observed in previous studies of the CS-processed HEA (Ref 18, 19). However, future work will involve a detail microstructural characterization of the deformation twinning and its mechanism of formation in the HEA during cold spraying.

The microstructure evolution—grain refinement and work hardening effects via the severe plastic deformation of the HEA during cold spraying resulted in the greater

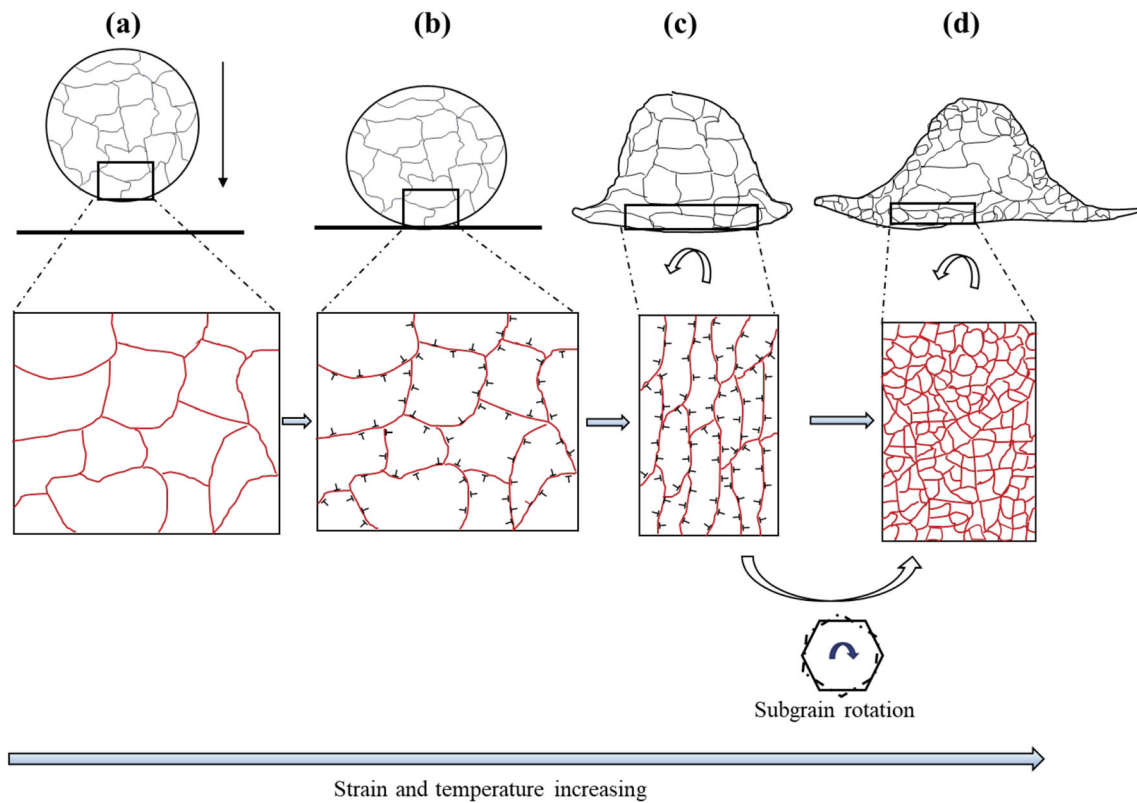


Fig. 16 The schematic explaining the mechanism of grain refinement at the bonding regions by dynamic recrystallization in the HEA particles during cold spraying: (a) homogeneous strain-free grain structure of the original powder before spraying; (b) upon impact, strain is induced due to deformation, and dislocations propagate; (c) with deformation going on, strain and dislocation density increases

resulting in the formation of elongated subgrains due to the accumulation and rearrangement of dislocations; (d) due to the severe deformation and strain increase, the elongated subgrains rotate, increasing in their misorientation angles to accommodate the strain, resulting in the formation of highly misoriented equiaxed fine grains

deposit nanohardness when compared to the sprayed powder. The measured nanohardness value increased by over 300%, from 1.16 GPa in the powder to 5.14 GPa in the deposit. Also, the analyzed average nanohardness near the particle–particle interfaces is greater than that of the central region by over (0.65 ± 0.04) GPa. The increased nanohardness near the impact interfaces can be attributed to a large number of grain boundaries and high dislocation densities induced by the cold spraying process. Grain refinement and high density of dislocations or GNDs in the deposit can act as obstacles for dislocation motion during indentation, resulting in dislocation pileups at grain boundaries leading to higher stress required to move dislocation through the pileups (Ref 60), therefore increasing the hardness value. Grain refinement contributes to the hardening of materials via the Hall–Petch effect (Ref 61), and the dislocation density contribution follows the Taylor hardening model (Ref 62).

Assuming a pore-free cold-sprayed HEA deposit, we can estimate as a first approximation the yield strength of the deposit using Eq 7, following the contributions of grain refinement and dislocation hardening.

$$\sigma_d = \sigma_0 + K_y/\sqrt{d} + M\alpha Gb\rho^{1/2} \tag{Eq 7}$$

where σ_d is the yield stress, σ_0 represents the intrinsic yield stress of the HEA material (taken as 125 MPa (Ref 5)), and K_y is the Hall–Petch coefficient. $K_y = 494 \text{ MPa}\cdot\mu\text{m}^{-1/2}$ has been reported for the CoCrFeNiMn HEA (Ref 5). Also, M is the Taylor factor (3.06 (Ref 63)), α is a constant taken as 0.4 (Ref 50), and G is the shear modulus (80 GPa for the HEA at room temperature (Ref 64)), b is the magnitude of the Burgers vector ($0.255 \times 10^{-3} \mu\text{m}$ at room temperature (Ref 65)), and ρ is the dislocation density taken from the EBSD analysis. Equation 7 gave an approximate yield stress σ_d of 647 MPa. The yield stress results from the grain refinement via dynamic recrystallization and dislocation density, is comparable to bulk HEA produced by either conventional additive manufacturing (601 MPa with $1 \mu\text{m}$ grain size) (Ref 66) but higher than as-cast (350 MPa with $4.4 \mu\text{m}$ grain size) (Ref 5). To compare the yield stress estimated from the above model with the measured hardness, we calculated the yield stress from the measured Vickers hardness (HV) of the HEA cold-sprayed deposit, using the equation

$\sigma_{HV} = (HV/3) \times 0.1^n$, as proposed by Cahoon et al. (Ref 67). The strain hardening exponent, n , of the HEA material is taken from Table 2. Thus, the measured microhardness values of 280 HV of the HEA cold-sprayed deposit correspond to approximate hardness-derived yield stress of 605 MPa. There is slight difference in the estimated yield stress from the contributing mechanisms and the hardness-derived yield stress. The discrepancies can be attributed to the effect of porosity and poor inter-particle bonding of the deposit during the microhardness indentation testing, and the approximation of the model employed. Future work will involve performing a standard tensile test to provide a more accurate representation of the tensile properties of the cold-sprayed HEA deposit.

Conclusions

A cold spraying process was employed to fabricate a thick deposit of CoCrFeNiMn HEA. The resulting microstructure from the ultra-high strain rate materials deposition process was characterized using SEM, XRD, EBSD and FEA tools, and the properties were measured using micro- and nano-indentation techniques. The main observations can be summarized as follows:

1. The CS-processed HEA deposit showed a heterogeneous spatial distribution of ultrafine and coarse grains at the splat interfaces and interiors. Significant grain refinement was obtained mainly at the splat impact interfaces within the deposit. The formation mechanism of the heterogeneous microstructure is attributed to adiabatic shear instability and dynamic recrystallization produced by subgrain rotation dominating the impact areas. Large strain and temperature gradients within the deformed particles, as evidenced by the FEA simulation, explain the heterogeneous microstructure formed.
2. The microstructural features in the cold-sprayed deposit contributed to the over 250% increase in the measured nanohardness value, from 1.16 GPa in the feedstock powder to 5.14 GPa in the HEA deposit. The increase in the hardness values was attributed to the grain refinement and high density of dislocations in the cold-sprayed HEA deposit. The high densities of grain boundaries and GNDs contributed to the greater nanohardness measured for the impact or bonding regions between particles when compared to that of the central regions of the particles.
3. A Taylor-based strength model that includes the contributions from the grain size and dislocations measured using EBSD predicted yield stress of 647 MPa for the HEA deposit. A hardness-derived yield

stress of 605 MPa was also estimated for the cold-sprayed HEA deposit. These theoretical yield stress values are comparable to the yield strength of bulk HEA produced by conventional AM methods; however, future work will involve tensile testing of a dense cold-sprayed deposit of the HEA.

Acknowledgment The authors acknowledge financial support from the Engineering and Physical Sciences Research Council [EP/V010093/1]. Cletus J. Akisin acknowledges financial support from the Petroleum Technology Development Fund, Nigeria. The authors also acknowledge John Kirk for supporting the cold spray experiments, Hannah Constantin for conducting the nanohardness indentation, and the Nanoscale and Microscale Research Centre (nmRC) at the University of Nottingham for using the SEM, XRD, and EBSD equipment.

Author Contribution CJA was involved in conceptualization, methodology, investigation, formal analysis, writing—original draft, and writing—review and editing. BD was involved in formal analysis and writing—review and editing. CB and FV were involved in supervision and writing—review and editing. M-SP was involved in resources and writing—review and editing. TH was involved in supervision, project administration, resources, conceptualization, and writing—review and editing.

Conflict of interest The authors declare that they have no known competing financial interests or personal relationships that could have appeared to influence the work reported in this paper.

Open Access This article is licensed under a Creative Commons Attribution 4.0 International License, which permits use, sharing, adaptation, distribution and reproduction in any medium or format, as long as you give appropriate credit to the original author(s) and the source, provide a link to the Creative Commons licence, and indicate if changes were made. The images or other third party material in this article are included in the article's Creative Commons licence, unless indicated otherwise in a credit line to the material. If material is not included in the article's Creative Commons licence and your intended use is not permitted by statutory regulation or exceeds the permitted use, you will need to obtain permission directly from the copyright holder. To view a copy of this licence, visit <http://creativecommons.org/licenses/by/4.0/>.

References

1. B. Cantor, I.T.H. Chang, P. Knight, and A.J.B. Vincent, Microstructural Development in Equiatomic Multicomponent Alloys, *Mater. Sci. Eng. A*, 2004, **375-377**, p 213-218.
2. J.W. Yeh, S.K. Chen, S.J. Lin, J.Y. Gan, T.S. Chin, T.T. Shun, C.H. Tsau, and S.Y. Chang, Nanostructured High-Entropy Alloys with Multiple Principal Elements: Novel Alloy Design Concepts and Outcomes, *Adv. Eng. Mater.*, 2004, **6(5)**, p 299-303.
3. Z. Li, S. Zhao, R.O. Ritchie, and M.A. Meyers, Mechanical Properties of High-Entropy Alloys with Emphasis on Face-Centered Cubic Alloys, *Progr. Mater. Sci.*, 2019, **102**, p 296-345.
4. S.W. Wu, G. Wang, Y.D. Jia, J. Yi, Q.J. Zhai, C.T. Liu, B.A. Sun, H.J. Chu, J. Shen, P.K. Liaw, and T.Y. Zhang, Enhancement of Strength-Ductility Trade-off in a High-Entropy Alloy through a Heterogeneous Structure, *Acta Mater.*, 2018, **2019(165)**, p 444-458.

5. F. Otto, A. Dlouhý, C. Somsen, H. Bei, G. Eggeler, and E.P. George, The Influences of Temperature and Microstructure on the Tensile Properties of a CoCrFeMnNi High-Entropy Alloy, *Acta Mater.*, 2013, **61**(15), p 5743-5755.
6. B. Gludovatz, A. Hohenwarther, D. Catoor, E.H. Chang, E.P. George, and R.O. Ritchie, A Fracture-Resistant High-Entropy Alloy for Cryogenic Applications, *Science*, 2014, **345**(6201), p 1153-1158.
7. Y.J. Kwon, J.W. Won, S.H. Park, J.H. Lee, K.R. Lim, Y.S. Na, and C.S. Lee, Ultrahigh-Strength CoCrFeMnNi High-Entropy Alloy Wire Rod with Excellent Resistance to Hydrogen Embrittlement, *Mater. Sci. Eng. A*, 2018, **732**, p 105-111. <https://doi.org/10.1016/j.msea.2018.06.086>
8. H. Shahmir, M.S. Mehranpour, S.A.A. Shams, and T.G. Langdon, Twenty Years of CoCrFeNiMn High-Entropy Alloy: Achieving Exceptional Mechanical Properties through Microstructure Engineering, *J. Mater. Res. Technol.*, 2022 <https://doi.org/10.1016/J.JMRT.2023.01.181>
9. F. Otto, A. Dlouhý, K.G. Pradeep, M. Kuběňová, D. Raabe, G. Eggeler, and E.P. George, Decomposition of the Single-Phase High-Entropy Alloy CrMnFeCoNi after Prolonged Anneals at Intermediate Temperatures, *Acta Mater.*, 2016, **112**, p 40-52.
10. B. Schuh, F. Mendez-Martin, B. Völker, E.P. George, H. Clemens, R. Pippan, and A. Hohenwarther, Mechanical Properties, Microstructure and Thermal Stability of a Nanocrystalline CoCrFeMnNi High-Entropy Alloy after Severe Plastic Deformation, *Acta Mater.*, 2015, **96**, p 258-268.
11. H. Shahmir, J. He, Z. Lu, M. Kawasaki, and T.G. Langdon, Effect of Annealing on Mechanical Properties of a Nanocrystalline CoCrFeNiMn High-Entropy Alloy Processed by High-Pressure Torsion, *Mater. Sci. Eng. A*, 2016, **676**, p 294-303.
12. H. Shahmir, T. Mousavi, J. He, Z. Lu, M. Kawasaki, and T.G. Langdon, Microstructure and Properties of a CoCrFeNiMn High-Entropy Alloy Processed by Equal-Channel Angular Pressing, *Mater. Sci. Eng. A*, 2017, **705**, p 411-419.
13. R. Singh, J. Kondás, C. Bauer, J. Cizek, J. Medricky, S. Csaki, J. Čupera, R. Procházka, D. Melzer, and P. Konopík, Bulk-like Ductility of Cold Spray Additively Manufactured Copper in the as-Sprayed State, *Addit. Manuf. Lett.*, 2022, **3**, p 100052.
14. C. Chen, Y. Xie, S. Yin, W. Li, X. Luo, X. Xie, R. Zhao, C. Deng, J. Wang, H. Liao, M. Liu, and Z. Ren, Ductile and High Strength Cu Fabricated by Solid-State Cold Spray Additive Manufacturing, *J. Mater. Sci. Technol.*, 2023, **134**, p 234-243. <https://doi.org/10.1016/J.JMST.2022.07.003>
15. Y. Zou, W. Qin, E. Irissou, J.G. Legoux, S. Yue, and J.A. Szpunar, Dynamic Recrystallization in the Particle/Particle Interfacial Region of Cold-Sprayed Nickel Coating: Electron Backscatter Diffraction Characterization, *Scr. Mater.*, 2009, **61**(9), p 899-902.
16. S. Yin, W. Li, B. Song, X. Yan, M. Kuang, Y. Xu, K. Wen, and R. Lupoi, Deposition of FeCoNiCrMn High Entropy Alloy (HEA) Coating via Cold Spraying, *J. Mater. Sci. Technol.*, 2019, **35**(6), p 1003-1007.
17. A. Silvello, P. Cavaliere, S. Yin, R. Lupoi, I. Garcia Cano, and S. Dosta, Microstructural, Mechanical and Wear Behavior of HVOF and Cold-Sprayed High-Entropy Alloys (HEAs) Coatings, *J. Therm. Spray Technol.*, 2022 <https://doi.org/10.1007/s11666-021-01293-w>
18. R. Nikbakht, M. Saadati, T.-S. Kim, M. Jahazi, H.S. Kim, and B. Jodoin, Cold Spray Deposition Characteristic and Bonding of CrMnCoFeNi High Entropy Alloy, *Surf. Coat. Technol.*, 2021 <https://doi.org/10.1016/J.SURFCOAT.2021.127748>
19. R. Nikbakht, C.V. Cojocar, M. Aghasibeig, É. Irissou, T.-S. Kim, H.S. Kim, and B. Jodoin, Cold Spray and Laser-Assisted Cold Spray of CrMnCoFeNi High Entropy Alloy Using Nitrogen as the Propelling Gas, *J. Therm. Spray Technol.*, 2022 <https://doi.org/10.1007/s11666-022-01361-9>
20. S. Feng, S. Guan, W.A. Story, J. Ren, S. Zhang, A. Te, M.A. Gleason, J. Heelan, C. Walde, A. Birt, K.L. Tsakopoulos, D.L. Cote, W. Kapalczynski, A.T. Naardi, V.K. Champagne, M.J. Siopis, and W. Chen, Cold Spray Additive Manufacturing of CoCrFeNiMn High-Entropy Alloy: Process Development, Microstructure, and Mechanical Properties, *J. Thermal Spray Technol.*, 2022 <https://doi.org/10.1007/s11666-022-01374-4>
21. R.C. Dykhuizen and M.F. Smith, Gas Dynamic Principles of Cold Spray, *J. Therm. Spray Technol.*, 1998, **7**(2), p 205-212.
22. T.H.V. Steenkiste, J.R. Smith, and R.E. Teets, Aluminum Coatings via Kinetic Spray with Relatively Large Powder Particles, *Surf. Coat. Technol.*, 2002, **154**(2-3), p 237-252.
23. A. Valente, D. Gitardi, and E. Carpanzano, Highly Efficient Compact Cold Spray System for In-Situ Repairing of Stainless Steel Material Components, *CIRP Ann.*, 2020, **69**(1), p 181-184. <https://doi.org/10.1016/j.cirp.2020.04.095>
24. V. Champagne and D. Helfritsch, Critical Assessment 11: Structural Repairs by Cold Spray, *Mater. Sci. Technol.*, 2015, **31**(6), p 627-634.
25. V.K. Champagne, The Repair of Magnesium Rotorcraft Components by Cold Spray, *J. Fail. Anal. Prev.*, 2008, **8**(2), p 164-175. <https://doi.org/10.1007/s11668-008-9116-y>
26. S. Yin, H.L. Liao, and X.F. Wang, Euler Based Finite Element Analysis on High Velocity Impact Behaviour in Cold Spraying, *Surf. Eng.*, 2014, **30**(5), p 309-315. <https://doi.org/10.1179/1743294413Y.0000000240>
27. H. Assadi, F. Gärtner, T. Stoltenhoff, and H. Kreye, Bonding Mechanism in Cold Gas Spraying, *Acta Mater.*, 2003, **51**(15), p 4379-4394. [https://doi.org/10.1016/S1359-6454\(03\)00274-X](https://doi.org/10.1016/S1359-6454(03)00274-X)
28. P.C. King, G. Bae, S.H. Zahiri, M. Jahedi, and C. Lee, An Experimental and Finite Element Study of Cold Spray Copper Impact Onto Two Aluminum Substrates, *J. Thermal Spray Technol.*, 2010, **19**, p 620-634.
29. G. Bae, S. Kumar, S. Yoon, K. Kang, H. Na, H.J. Kim, and C. Lee, Bonding Features and Associated Mechanisms in Kinetic Sprayed Titanium Coatings, *Acta Mater.*, 2009, **57**(19), p 5654-5666.
30. T. Schmidt, F. Gärtner, H. Assadi, and H. Kreye, Development of a Generalized Parameter Window for Cold Spray Deposition, *Acta Mater.*, 2006, **54**(3), p 729-742.
31. W.Y. Li, C. Zhang, C.J. Li, and H. Liao, Modeling Aspects of High Velocity Impact of Particles in Cold Spraying by Explicit Finite Element Analysis, *J. Therm. Spray Technol.*, 2009, **18**(5-6), p 921-933. <https://doi.org/10.1007/s11666-009-9325-2>
32. C.J. Akisin, C.J. Bennett, F. Venturi, H. Assadi, and T. Hussain, Numerical and Experimental Analysis of the Deformation Behavior of CoCrFeNiMn High Entropy Alloy Particles Onto Various Substrates during Cold Spraying, *J. Therm. Spray Technol.*, 2022 <https://doi.org/10.1007/s11666-022-01377-1>
33. W. Pantleon, Resolving the Geometrically Necessary Dislocation Content by Conventional Electron Backscattering Diffraction, *Scr. Mater.*, 2008, **58**(11), p 994-997.
34. W.C. Oliver and G.M. Pharr, Measurement of Hardness and Elastic Modulus by Instrumented Indentation: Advances in Understanding and Refinements to Methodology, *J. Mater. Res.*, 2004, **19**(1), p 3-20. <https://doi.org/10.1557/jmr.2004.19.1.3>
35. T.A. Owoseni, M. Bai, N. Curry, E.H. Lester, D.M. Grant, and T. Hussain, Residual Stress Measurement of Suspension HVOF-Sprayed Alumina Coating Via a Hole-Drilling Method, *J. Therm. Spray Technol.*, 2020, **29**(6), p 1339-1350. <https://doi.org/10.1007/s11666-020-01072-z>
36. B. Yildirim, S. Muftu, and A. Gouldstone, Modeling of High Velocity Impact of Spherical Particles, *Wear*, 2011, **270**(9-10), p 703-713.

37. T. Schmidt, H. Assadi, F. Gärtner, H. Richter, T. Stoltenhoff, H. Kreye, and T. Klassen, From Particle Acceleration to Impact and Bonding in Cold Spraying, *J. Therm. Spray Technol.*, 2009, **18**(5–6), p 794–808.
38. W.Y. Li and W. Gao, Some Aspects on 3D Numerical Modeling of High Velocity Impact of Particles in Cold Spraying by Explicit Finite Element Analysis, *Appl. Surf. Sci.*, 2009, **255**(18), p 7878–7892.
39. G.R. Johnson and W.H. Cook, Fracture Characteristics of Three Metals Subjected to Various Strains, Strain Rates, Temperatures and Pressures, *Eng. Fract. Mech.*, 1985, **21**(1), p 31–48. [https://doi.org/10.1016/0013-7944\(85\)90052-9](https://doi.org/10.1016/0013-7944(85)90052-9)
40. M. Grujicic, B. Pandurangan, C.F. Yen, and B.A. Cheeseman, Modifications in the AA5083 Johnson-Cook Material Model for Use in Friction Stir Welding Computational Analyses, *J. Mater. Eng. Perform.*, 2012, **21**(11), p 2207–2217.
41. S. Yin, M. Meyer, W. Li, H. Liao, and R. Lupoi, Gas Flow, Particle Acceleration, and Heat Transfer in Cold Spray: A Review, *J. Therm. Spray Technol.*, 2016, **25**(5), p 874–896.
42. H. Fukunuma, N. Ohno, B. Sun, and R. Huang, In-flight Particle Velocity Measurements with DPV-2000 in Cold Spray, *Surf. Coat. Technol.*, 2006, **201**(5), p 1935–1941.
43. M. Bray, A. Cockburn, and W. O'Neill, The laser-assisted cold spray process and deposit characterisation, *Surf. Coat. Technol.*, 2009, **203**(19), p 2851–2857.
44. S. Özbilen, Satellite Formation Mechanism in Gas Atomized Powders, *Powder Metall.*, 1999, **42**(1), p 70–78. <https://doi.org/10.1179/pom.1999.42.1.70>
45. H. Jones, Microstructure of Rapidly Solidified Materials, *Mater. Sci. Eng.*, 1984, **65**(1), p 145–156.
46. M. Laurent-Brocq, A. Akhatova, L. Perrière, S. Chebini, X. Sauvage, E. Leroy, and Y. Champion, Insights into the Phase Diagram of the CrMnFeCoNi High Entropy Alloy, *Acta Mater.*, 2015, **88**, p 355–365. <https://doi.org/10.1016/j.actamat.2015.01.068>
47. V.K. Champagne, D.J. Helfritsch, M.D. Trexler, and B.M. Gabriel, The Effect of Cold Spray Impact Velocity on Deposit Hardness, *Model. Simul. Mater. Sci. Eng.*, 2010, **18**(6), p 8.
48. R. Chakrabarty and J. Song, A Modified Johnson-Cook Material Model with Strain Gradient Plasticity Consideration for Numerical Simulation of Cold Spray Process, *Surf. Coat. Technol.*, 2020, **397**, p 125981. <https://doi.org/10.1016/j.surfcoat.2020.125981>
49. J.-E. Ahn, Y.-K. Kim, S.-H. Yoon, and K.-A. Lee, Tuning the Microstructure and Mechanical Properties of Cold Sprayed Equiatomic CoCrFeMnNi High-Entropy Alloy Coating Layer, *Met. Mater. Int.*, 2020 <https://doi.org/10.1007/s12540-020-00886-4>
50. G. Laplanche, A. Kostka, O.M. Horst, G. Eggeler, and E.P. George, Microstructure Evolution and Critical Stress for Twinning in the CrMnFeCoNi High-Entropy Alloy, *Acta Mater.*, 2016, **118**, p 152–163.
51. G.Y. Chin, W.F. Hosford, and D.R. Mendorf, Accommodation of Constrained Deformation in fcc Metals by Slip and Twinning, *Proc. R. Soc. London A Math. Phys. Sci.*, 1969, **309**(1499), p 433–456.
52. M. Naeem, H. He, S. Harjo, T. Kawasaki, F. Zhang, B. Wang, S. Lan, Z. Wu, Y. Wu, Z. Lu, C.T. Liu, and X.L. Wang, Extremely High Dislocation Density and Deformation Pathway of CrMnFeCoNi High Entropy Alloy at Ultralow Temperature, *Scr. Mater.*, 2020, **188**, p 21–25.
53. G. Bae, J.I. Jang, and C. Lee, Correlation of Particle Impact Conditions with Bonding, Nanocrystal Formation and Mechanical Properties in Kinetic Sprayed Nickel, *Acta Mater.*, 2012, **60**(8), p 3524–3535. <https://doi.org/10.1016/j.actamat.2012.03.001>
54. B. Dovggy, A. Piglione, P.A. Hooper, and M.S. Pham, Comprehensive Assessment of the Printability of CoNiCrFeMn in Laser Powder Bed Fusion, *Mater. Des.*, 2020, **194**, p 108845.
55. C. Haase, F. Tang, M.B. Wilms, A. Weisheit, and B. Hallstedt, Combining Thermodynamic Modeling and 3D Printing of Elemental Powder Blends for High-Throughput Investigation of High-Entropy Alloys—Towards Rapid Alloy Screening and Design, *Mater. Sci. Eng. A*, 2017, **688**, p 180–189. <https://doi.org/10.1016/j.msea.2017.01.099>
56. Z. Li, S. Zhao, S.M. Alotaibi, Y. Liu, B. Wang, and M.A. Meyers, Adiabatic Shear Localization in the CrMnFeCoNi High-Entropy Alloy, *Acta Mater.*, 2018, **151**, p 424–431. <https://doi.org/10.1016/j.actamat.2018.03.040>
57. J. Wu, H. Fang, S. Yoon, H. Kim, and C. Lee, The Rebound Phenomenon in Kinetic Spraying Deposition, *Scr. Mater.*, 2006, **54**, p 665–669.
58. P. Yu, N. Fan, Y. Zhang, Z. Wang, and W. Li, Microstructure Evolution and Composition Redistribution of FeCoNiCrMn High Entropy Alloy under Extreme Plastic Deformation, *Mater. Res. Lett.*, 2022 <https://doi.org/10.1080/21663831.2021.2023678>
59. M.A. Meyers, Y.B. Xu, Q. Xue, M.T. Pérez-Prado, and T.R. McNelley, Microstructural Evolution in Adiabatic Shear Localization in Stainless Steel, *Acta Mater.*, 2003, **51**(5), p 1307–1325.
60. B.B. Jung, H.K. Lee, and H.C. Park, Effect of Grain Size on the Indentation Hardness for Polycrystalline Materials by the Modified Strain Gradient Theory, *Int. J. Solids Struct.*, 2013, **50**(18), p 2719–2724.
61. W.H. Liu, Y. Wu, J.Y. He, T.G. Nieh, and Z.P. Lu, Grain Growth and the Hall-Petch Relationship in a High-Entropy FeCrNiCoMn Alloy, *Scr. Mater.*, 2013, **68**(7), p 526–529.
62. G.I. Taylor, Plastic strain in metals, in *Twenty-eighth May Lecture to the Institute of Metals*, 1938, p 307–325, <https://ci.nii.ac.jp/naid/10026664057/>. Accessed 28 July 2022.
63. W.F. Hosford, Mechanical Behavior of Materials, *Mech. Behav. Mater.*, 2005 <https://doi.org/10.1017/CBO9780511810930>
64. A. Haglund, M. Koehler, D. Catoor, E.P. George, and V. Kepens, Polycrystalline Elastic Moduli of a High-Entropy Alloy at Cryogenic Temperatures, *Intermetallics*, 2015, **58**, p 62–64.
65. G. Laplanche, O. Horst, F. Otto, G. Eggeler, and E.P. George, Microstructural Evolution of a CoCrFeMnNi High-Entropy Alloy after Swaging and Annealing, *J. Alloys Compd.*, 2015, **647**, p 548–557.
66. R. Li, P. Niu, T. Yuan, P. Cao, C. Chen, and K. Zhou, Selective Laser Melting of an Equiatomic CoCrFeMnNi High-Entropy Alloy: Processability, Non-equilibrium microstructure and Mechanical Property, *J. Alloys Compd.*, 2018, **746**, p 125–134.
67. J.R. Cahoon, W.H. Broughton, and A.R. Kutzak, The Determination of Yield Strength from Hardness Measurements, *Metal. Trans.*, 1971, **2**(7), p 1979–1983. <https://doi.org/10.1007/BF02913433>

Publisher's Note Springer Nature remains neutral with regard to jurisdictional claims in published maps and institutional affiliations.